

# **Two-Neutron Correlations in the Photofission of $^{238}\text{U}$**

phd Thesis

Jeffrey S. Burggraf

October 19, 2018

Advisor: Prof. Dr. D. S. Dale  
Department of Physics, Idaho State University



---

## Abstract

In the fission of actinides, the nearly back-to-back motion of the fission fragments has a strong effect on the kinematics of fission neutrons. This effect is seen in the two-neutron opening angle distributions of correlated neutron pairs from the same fission event in which a favoring of opening angles near  $0^\circ$  and  $180^\circ$  is observed. The purpose of this work is to measure the two-neutron opening angle and energy correlations in the photofission of  $^{238}\text{U}$ . As of this writing, correlated two-neutron opening angle distributions have been measured using neutrons from spontaneous and neutron-induced fission of actinides. This work is the first to report such a measurement using photofission, and will provide useful experimental input for photofission models used in codes such as MCNP and FREYA.

Fission is induced using bremsstrahlung photons produced via a low duty factor, pulsed, linear electron accelerator. The photon beam impinges upon a  $^{238}\text{U}$  target that is surrounded by a large neutron scintillation detection system capable of measuring particle position and time of flight, from which two-neutron opening angle and energy is calculated. Two-neutron angular correlations are determined by taking the ratio of the opening angle distribution of correlated neutron pairs to that of uncorrelated neutrons pairs in which the neutrons of each pair were detected during different accelerator pulses. This technique gives a self-contained result which greatly diminishes effects due to detector efficiencies, acceptance, and experimental drifts.

The angular correlation of neutrons from the photofission of  $^{238}\text{U}$  shows a high dependence on neutron energy and a slight dependence on the angle of the emitted neutrons with respect to the incoming photon beam. Angular correlations were also measured using neutrons from the spontaneous fission of  $^{252}\text{Cf}$ , showing good agreement with past measurements. An

---

anomalous decline in two-neutron yield was observed for opening angles near  $180^\circ$ .

---

# Contents

---

<b>Contents</b>	<b>iii</b>
<b>1 Introduction</b>	<b>1</b>
1.1 Introduction . . . . .	1
1.1.1 Fission and Neutron Correlations . . . . .	1
1.1.2 Connection to Physics . . . . .	3
1.1.3 Past Measurements, Spontaneous and Neutron Induced Fission . . . . .	4
<b>2 Methods</b>	<b>7</b>
2.1 Experimental Setup . . . . .	7
2.1.1 Detectors . . . . .	7
2.1.2 Detector Shielding . . . . .	10
2.1.3 Bremsstrahlung Photon Beam . . . . .	12
2.2 Experimental Methods . . . . .	13
2.2.1 Particle Time of Flight and Energy Determination . . . . .	13
2.2.2 Particle Position Reconstruction . . . . .	16
2.2.3 DU Target . . . . .	19
2.2.4 Electronics . . . . .	19
2.2.5 Measurements with $^{252}\text{Cf}$ . . . . .	21
2.3 Analysis . . . . .	22
2.3.1 Cancelation of Detector Efficiencies, Drifts, and Geometric Phase Space . . . . .	22
2.3.2 Subtraction of Accidental Coincidences . . . . .	26
<b>3 Discussion of Experimental Errors</b>	<b>31</b>
3.1 Random Errors . . . . .	31

## CONTENTS

---

3.1.1	Resolution of measurement . . . . .	31
3.1.2	Counting error . . . . .	33
3.2	Detector Cross-talk . . . . .	33
3.2.1	Cross-talk Simulation . . . . .	34
3.2.2	Neutron Scattering within Target . . . . .	37
<b>4</b>	<b>Results</b>	<b>41</b>
4.1	Asymmetries in $\theta_{abs}$ of Neutron Singles . . . . .	41
4.2	Two-neutron opening Angle Correlations . . . . .	43
4.3	Correlation of $\theta_{abs}$ . . . . .	52
4.4	Rates . . . . .	54
<b>5</b>	<b>Concluding Remarks</b>	<b>57</b>

## Chapter 1

---

# Introduction

---

## 1.1 Introduction

### 1.1.1 Fission and Neutron Correlations

The photofission reaction occurs during the de-excitation of a nucleus after the absorption of a photon. For photon energies between 6 and 25 MeV, this absorption occurs primarily via the giant dipole resonance (GDR). One distinct and useful aspect of photofission, particularly when compared to neutron-induced fission, is the simple set of selection rules for the transfer of angular momentum. In photofission, there is a relatively low transfer of angular momentum to the nucleus, and as a result photon absorption occurs primarily via E1 absorption and to a lesser extent E2 absorption. Because of this selectivity, photofission is commonly used as a means to study sub-nuclear structures and the fundamentals of the fission process. For even-even nuclei,  $J^\pi$  values of the excited state are restricted to the electric dipole ( $1^-$ ) and electric quadrupole ( $2^+$ ) states, which gives rise to anisotropies in the fission fragment angular distribution that are far more pronounced than for other types of fission [?]. Detailed studies of the dynamics of fission provide significant insight into the fundamental physics of this process, and have the potential to shed light on

## 1. INTRODUCTION

---

model parameters needed for a comprehensive theoretical description of fission. Fission neutron emission can be classified into two categories, depending on the time of emission: delayed and prompt. Delayed neutrons account for only  $\sim 1\%$  of total neutron emission in actinide photofission [?]. Delayed neutrons are not important to this study, and this measurement is insensitive to them. Prompt fission neutrons are defined as neutrons that are emitted either immediately after ( $< 10^{-14}$  seconds) fission or during the scission of the nucleus, and account for the remaining  $\sim 99\%$  of neutron emission [?]. Prompt fission neutron production occurs by means of two distinct mechanisms. The dominant mechanism is neutron emission from the fully accelerated fragments. The second mechanism, referred to as *early* or *scission* neutron emission, is the emission of neutrons during either the scission of the nucleus, or the acceleration of the fission fragments. Both cases are described below.

A large number of past studies have established that the majority of prompt fission neutrons (80%–98%) are emitted from the fully accelerated fragments, while the remaining 2%–20% percent are scission neutrons [?]. The nature of scission neutrons has remained elusive since their first tentative observation in 1962 by Bowman *et al.* [?]. Models of prompt neutron emission in binary fission are based mainly on observations of neutron angular distributions relative to the fission axis—the axis along which the fragments travel in the center of momentum frame. Another observational input for prompt neutron modeling is the neutron-neutron opening angle distribution of correlated neutron pairs, as seen in the lab frame, hereafter denoted  $\theta_{nn}$ . Because fission neutrons are predominantly emitted from the fully accelerated fragments, the distribution of  $\theta_{nn}$  is reflective of the underlying fundamental fission kinematics. There are, on average, about 2 or 3 neutrons released per fission, depending on the isotope

and how the fission is induced. It has been shown that neutrons released from the fully accelerated fission fragments are evaporated isotropically in the fragment's rest frame, where they are emitted at speeds comparable to that of the fragments themselves [?]. This leads to the well-known U-shaped distribution in  $\theta_{nn}$ , which has been reported in studies of neutron-induced, spontaneous, and, in this study, photon-induced fission.

The U-shaped distribution of  $\theta_{nn}$  can be understood as the result of the boost provided to the neutrons by the fission fragments in binary fission. Due to the conservation of momentum, the fully accelerated fission fragments are traveling nearly back-to-back, and neutrons emitted from different fragments are boosted in opposite directions, and neutrons emitted from the same fragment are boosted in the same direction. Thus, if the velocity of the fission fragments is large enough to account for a significant portion of the kinetic energy of fission neutrons, then neutron pairs emitted from the accelerated fragments will experience a favoring of opening angles near  $0^\circ$  and  $180^\circ$ , and a suppression of opening angles around  $90^\circ$ . The favoring of large and small opening angles shows a strong dependence on neutron energy, because neutrons with higher energy are more likely to have been emitted along the same direction of the fission fragments.

### 1.1.2 Connection to Physics

Two-neutron correlations in fission, and particularly photon-induced fission, are expected to shed light on several fundamental aspects of the fission process including the neutron multiplicity distributions associated with the light and heavy fission fragments, the nuclear temperatures of the fission fragments, and the mass distribution of the fission fragments as a function of energy released.

## 1. INTRODUCTION

---

In addition, the unique kinematics of fission and the resulting two-neutron correlations have the potential to be the basis for a new tool to detect fissiable materials [?]. Furthermore, two-neutron opening angle measurements are useful for the study of scission neutrons. Scission neutrons are thought to be emitted isotropically in the lab frame, and so they have the effect of flattening out the U-shaped two-neutron opening angle distribution. Because of this effect, these measurements add to the growing breadth of nuclear data needed to confirm the exact extent of the scission-neutron component in fission, which remains an open problem in nuclear physics.

### 1.1.3 Past Measurements, Spontaneous and Neutron Induced Fission

As of this writing, tabulated data for photofission is far scarcer than for neutron induced fission. The first measurement of the angular correlation among coincident neutrons from fission was performed by Debenedetti *et al.* [?] in 1948 from neutron induced fission of  $^{235}\text{U}$ . The next measurement of this type was performed by Pringle and Brooks in 1975 [?], in which neutrons emitted from the spontaneous fission (SF) of  $^{252}\text{Cf}$  were found to have high coincidence rates at small opening angles near  $0^\circ$  and large opening angles near  $180^\circ$ . In order to produce a result that is insensitive to the effects of detector geometry and efficiency, the present work uses techniques similar to reference [?], in which a ratio is taken between a correlated opening angle distribution and an uncorrelated opening angle distribution. To date, numerous measurements of two-neutron angular correlation using  $^{252}\text{Cf}$  have been performed [?, ?, ?]. This makes  $^{252}\text{Cf}$  a good benchmark for two-neutron angular correlation measurements. See Fig. 11, which compares measurements in this work to past

measurements of two-neutron correlations in the SF of  $^{252}\text{Cf}$ . Correlated two-neutron measurements have also been performed using thermal induced fission of  $^{235}\text{U}$ ,  $^{233}\text{U}$ , and  $^{239}\text{Pu}$  [?].

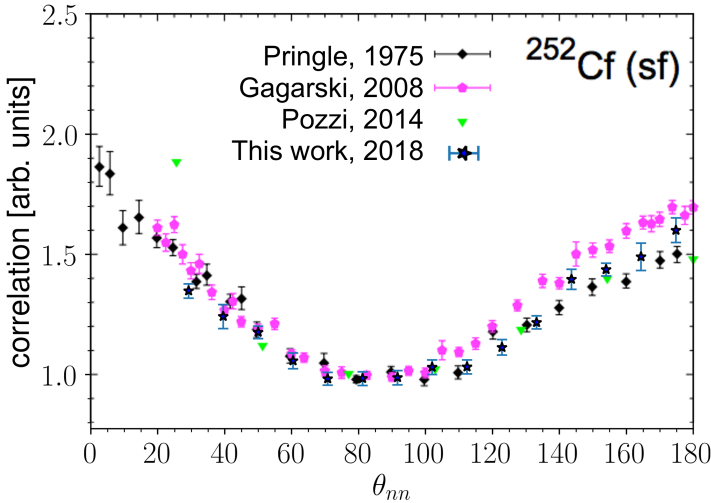


Figure 11:  $\theta_{nn}$  distribution from the SF of  $^{252}\text{Cf}$ . The neutron detection threshold for Pringle [?], Gagarski [?], and Pozzi [?] is 0.425 MeV, 0.425 MeV, and 0.7 MeV, respectively, and for this work is 0.5 MeV.



## Chapter 2

---

# Methods

---

### 2.1 Experimental Setup

The experiment was carried out at the Idaho Accelerator Center (IAC), using their fast-pulsed linear accelerator, which is an L-band frequency (1300 MHz) accelerator. It is capable of pulse widths ranging from 50 ps to 2  $\mu$ s with a maximum energy of 44 MeV. See section 2.1.3 for the accelerator parameters used during the experiment. Figure 21 shows a top down diagram of the experimental arrangement.

#### 2.1.1 Detectors

The detection system measures neutron position and time of flight (ToF), which is defined as the time taken for a particle to travel from the target to any detector. The purpose of ToF measurement is to calculate the kinetic energy of detected neutrons and to distinguish between photons and neutrons. The neutron detection system consists of fourteen shielded scintillators arranged in a ring around the target (see Fig. 22). The scintillators were made from Polyvinyl Toluene (PVT), an organic plastic scintillator. Attached to both ends of each scintillator are 10-cm long, non-scintillating, ultra-violet transmitting

## 2. METHODS

---

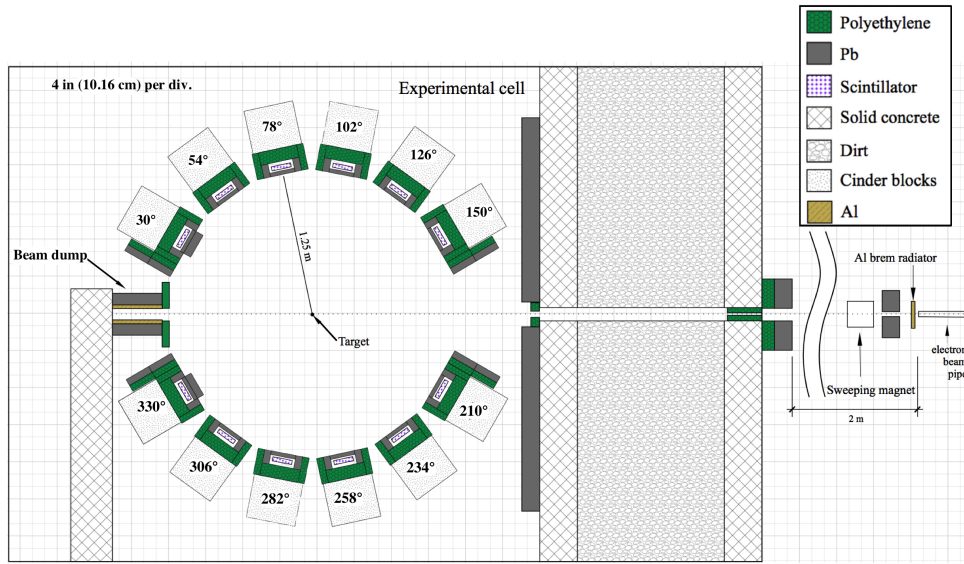


Figure 21: To-scale, top down diagram of the experimental setup. An electron beam impinges upon a 3.8 cm thick Al radiator, and the resulting bremsstrahlung beam enters the experimental cell from the top. The supporting structure for each detector has been labeled according to the angle, in degrees, between the center of each detector and direction of the incoming photon beam.

light guides. A Hamamatsu 580-17 photomultiplier (PMT) tube is fixed to each light guide using optical glue. In order to increase the chance that scintillation light remains inside the scintillator, they were polished to remove micro-imperfections and were wrapped in reflective aluminized mylar.

Ten out of the fourteen scintillators had dimensions of  $76.2 \times 15.2 \times 3.8 \text{ cm}^3$ . The remaining four scintillators, with dimensions of  $25.4 \times 15.2 \times 3.8 \text{ cm}^3$ , were located at  $30^\circ$  and  $330^\circ$  with respect to the beam. These scintillators were segmented in order to address very high photon detection rates resulting from the forward scattering of photons from the target. Prior to segmentation, a photon was registered in these detectors nearly every pulse, and because the electronics were operated in single hit mode, the detection of a photon leaves the detector unable to detect subsequent neutrons, reducing the neutron detection efficiency to nearly 0%. After segmentation, the photon detection rate fell

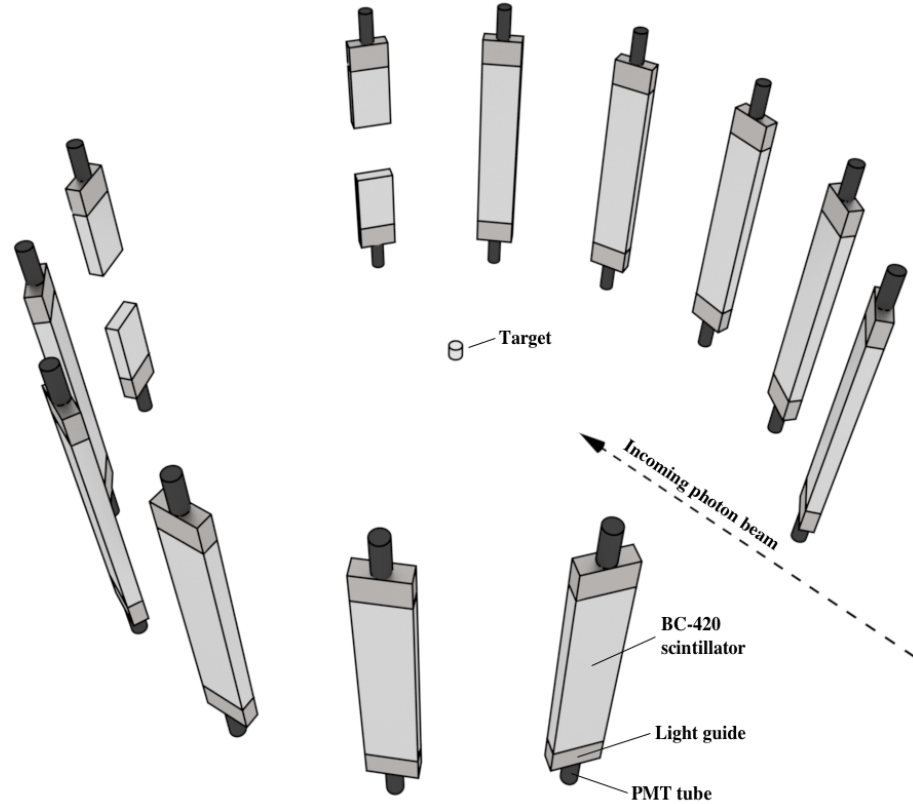


Figure 22: 3-D render of the bare, unshielded scintillators, along with PMTs and light guides.

to 0.5 photons per pulse, greatly improving detector live-time. The detectors at  $\pm 30$  degrees also differ from the rest in that they were instrumented with only a single PMT, and therefore have a lower position/energy resolution than the others. In order to test for systematic errors that may have resulted from the use of the segmented detectors, opening angle measurements were compared with and without their use, and the differences were well within experimental errors.

The relative efficiencies of the neutron detectors as a function of neutron energy were calculated by diving measured and theoretical yields from the SF of  $^{252}\text{Cf}$ . The results are shown in Fig. 23, which uses the aggregate of events from all detectors, and in Fig. 24, which shows it for each detector individually.

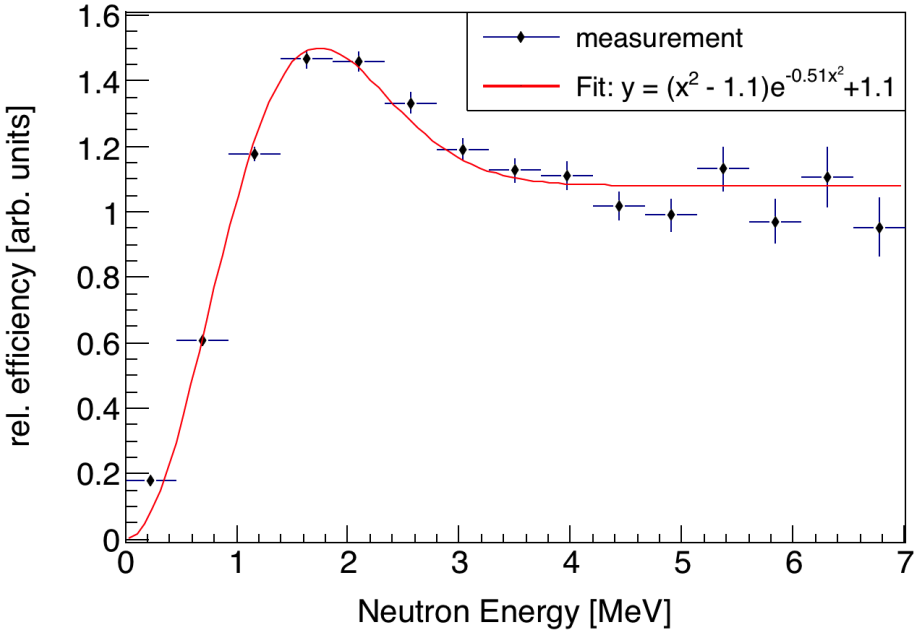


Figure 23: The relative efficiency of the neutron detection system as a function of neutron energy is calculated by dividing the measured energy distribution by the theoretical energy distribution of neutrons from the SF of  $^{252}\text{Cf}$ .

See section 2.3 for a discussion on how the effects of detector efficiency are accounted for in this work.

### 2.1.2 Detector Shielding

The detector shielding, depicted in Fig. 25, was constructed using lead and polyethylene with the aim of reducing cross-talk, the detection of photons, and noise. Pb was used to attenuate photons, but has the side effects of neutron scattering and reduced neutron detection efficiency. If a neutron scatters prior to being detected, the opening angle reconstruction and ToF calculation will be incorrect because both assume that detected neutrons travel a straight path from the target to the detector. 2.5 cm of Pb was placed along the front face of the scintillators, which is enough to largely reduce photon detection rates, and, according to an MCNP simulation, leads to a root-mean-square error in opening angle and ToF of  $1^\circ$  and 0.3 ns, respectively, due to neutron elastic

## 2.1. Experimental Setup

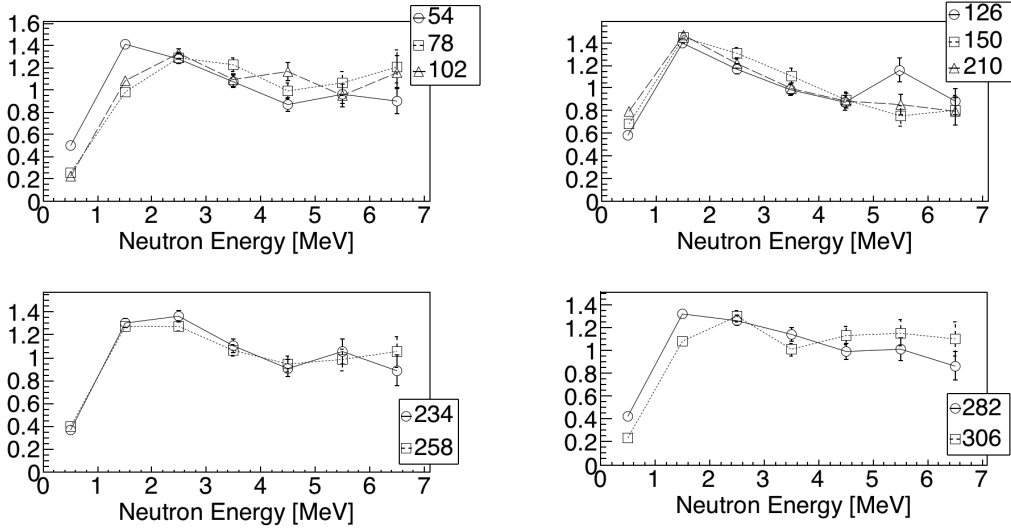


Figure 24: The neutron detection efficiency as a function of neutron energy varies among the detectors, which are labeled in this figure according to the angle each detector from the direction of the Bremsstrahlung photon beam.

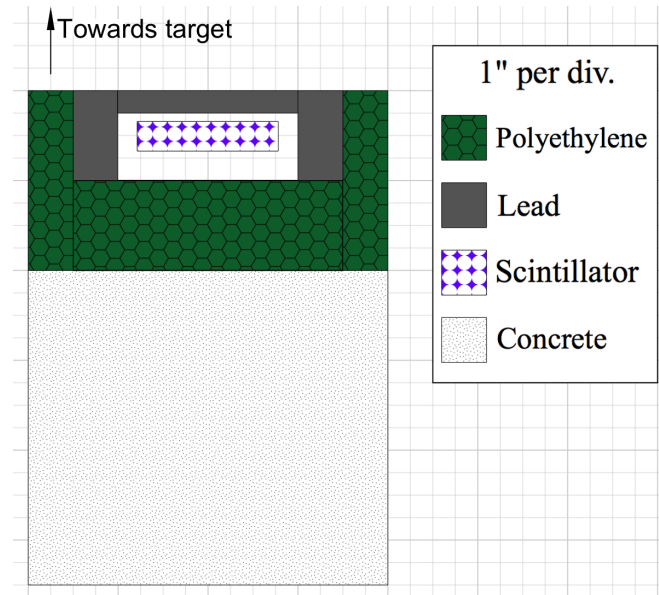


Figure 25: Detector shielding was designed to reduce the detection of photons, room return, and detector cross-talk.

## 2. METHODS

---

scattering. The sides of each scintillator were shielded with 5 cm of Pb to attenuate photons, followed by 5 cm of polyethylene to reduce the chance of neutron cross-talk. Also in order to minimize cross-talk, Pb was not placed behind the scintillators after an MCNP-POLIMI simulation indicated it would occur at significant rates otherwise. Instead, 10 cm of polyethylene was placed behind the scintillators. For a more detailed discussion about the issue of cross-talk, see section 3.2.

### 2.1.3 Bremsstrahlung Photon Beam

In order to ensure that all correlated neutrons produced are due to fission, the bremsstrahlung end-point was set to 10.5 MeV, safely below the  $(\gamma, 2n)$  threshold of 11.28 MeV for  $^{238}\text{U}$ . Al was chosen for a bremsstrahlung radiator, because Al has a neutron knockout threshold above the energy of the electron beam, which ensured that the radiator would not be a source of fast neutrons with the potential to interfere with the experiment. Downstream from the bremsstrahlung radiator is a sweeping magnet to remove charged particles from the photon beam. Next, the beam traveled through a series of polyethylene and lead collimators and into the experimental cell in which the target was located (see Fig. 21). Figure 26 shows the energy distribution of photons that reach the target according to an MCNP simulation that included the production and collimation of the bremsstrahlung photon beam.

The electron beam pulse width was set to 3 ns with a repetition rate of 240 Hz and a 1.1 A peak current. The 3 ns pulse width is not a large source of uncertainty in the measurement of neutron time of flight (ToF), because neutrons had a median ToF of  $\approx$ 80 ns.

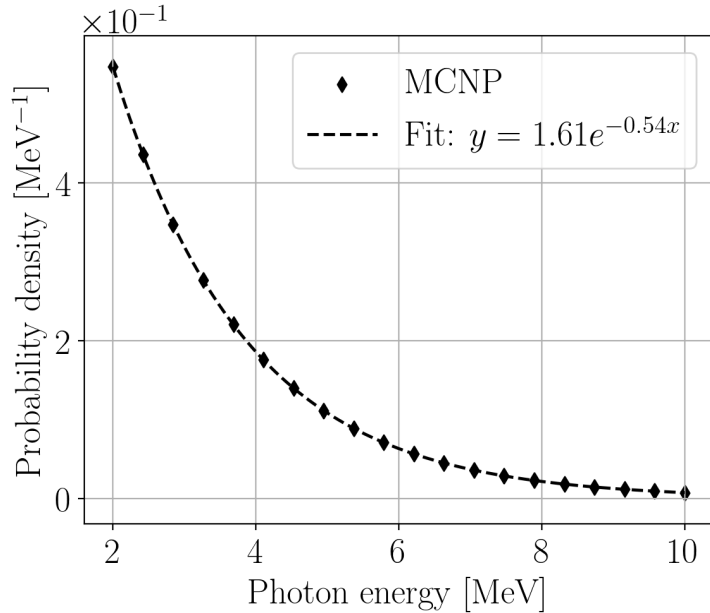


Figure 26: MCNP simulation of the energy distribution of photons that are incident on the fission target.

## 2.2 Experimental Methods

### 2.2.1 Particle Time of Flight and Energy Determination

The ToF of detected particles is used to distinguish between neutrons and photons and to determine neutron energy. A particle's reconstructed position is used to determine direction of motion, which is then used to calculate the opening angle between pairs of detected particles. Data from all PMTs is read out each pulse, and if multiple signals are received from a given PMT, only the first is accepted because subsequent signals have a restricted timing window due to dead-time. Position and ToF are each determined using the timing of coincident signals from both PMTs of a detector.

The sum of the times required for scintillation light to travel from the point of scintillation to both PMTs is equal to the time required for the light to travel the full length of the scintillator, which is a constant. This is supported by data,

## 2. METHODS

---

shown in Fig. 27, taken using a collimated  $^{60}\text{Co}$  source to generate photon events at several different locations along the scintillator, all which have equal ToF. In Fig. 27(a), it can be seen that the time required for the scintillation light to propagate through the scintillator effects the timing of each PMT alone, however, the average of the times of both PMTs is a constant, unaffected by the location at which the particle undergoes scintillation. With an effective index of refraction of 2.0, light takes 5 ns to travel the scintillator's full length. For this reason, taking the average of signals from two PMTs is advantageous because it removes a roughly 5 ns timing error that would otherwise exist due to the time required for scintillation light to propagate through the scintillator. The requirement that there be coincident events in both a detector's PMT is also beneficial because it reduces noise.

ToF is calculated by the following expression:

$$\text{ToF} = t_{\text{avg}}^{\text{PMTs}} - t_{\text{beam}} + C$$

where  $t_{\text{avg}}^{\text{PMTs}}$  is the average of the times of signals from both PMTs of a scintillator,  $t_{\text{beam}}$  is the time of a signal provided by the accelerator at the beginning of each pulse, and  $C$  is a constant timing offset determined by observing photons that scatter from the target. Any process that produces a timing delay that does not change from pulse to pulse contributes to  $C$ , for example:

- the time required for photons to travel from the bremsstrahlung radiator to the target
- the propagation of signals through the wires connecting the PMTs
- delays in the electronics
- the transit time in the PMTs.

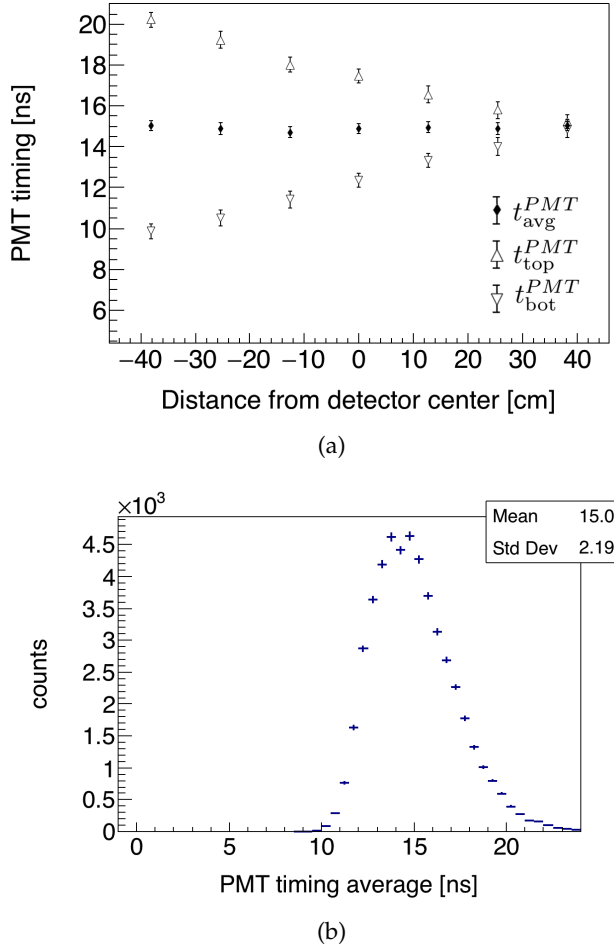


Figure 27: (a) A collimated  $^{60}\text{Co}$  source is used to produce photon events with constant ToF at seven locations along the detector. The average between the signals from both PMTs is virtually constant, thus the use of two PMTs removes timing error due to the time required for scintillation light to travel through the scintillator. Error bars are uncertainty in the mean of each data point. (b) The uncertainty in ToF measurements is equal to the standard deviation of this histogram ( $\pm 2$  ns), since coincident photons from  $^{60}\text{Co}$  are emitted at the same time.

- the time required for scintillation light to propagate from the point of creation to both PMTs.

The value of  $C$  may be different for each detector, but this is not a problem because it can be determined accurately by comparing the timing spectra of a non-neutron producing target made from aluminum, to the spectra produced

## 2. METHODS

---

when no target is used. The difference between no target and aluminum target reveals a prominent peak due to photons that scatter from the aluminum target. Photons which scattered from the target must travel between 125 cm to 130 cm before reaching the face of any detector, depending on whether the photons reach the detector near the center or at the edge. The two extreme cases are 125 cm and 130 cm distances, for which light takes 4.0 ns and 4.3 ns to travel, respectively. The difference between these two times is negligible, so the ToF of photons that scatter from the target is assumed to be 4 ns. This fact, along with the prominent photon peak seen in the timing spectra, is used to calculate the value of  $C$  for each detector.

Under the assumption that neutrons travel to the detectors unimpeded, the calculation of neutron energy from ToF is straightforward. This assumption is validated through MCNP simulations that tested the frequency of the scattering of fission neutrons within the target and the shielding of the detectors, and is discussed in sections 2.2.3 and 2.1.1, respectively. Figure 28(a) shows the relationship between neutron energy and ToF, and Figure 28(b) shows the uncertainty in measured neutron energy according to the propagation of ToF measurement uncertainty through the calculation of neutron energy.

### 2.2.2 Particle Position Reconstruction

The detectors are not capable of measuring the position of a detected particle along the axes parallel to the detectors width (15.24 cm wide) and depth (3.81 cm deep), which contributes  $\pm 3^\circ$  to the total angular uncertainty. The position of a particle hit along the 76.2 cm length of the scintillator is calculated from the timing difference of signals from both of a detector's PMTs. Under the assumption that light travels at a constant velocity from some distance,  $x$ ,

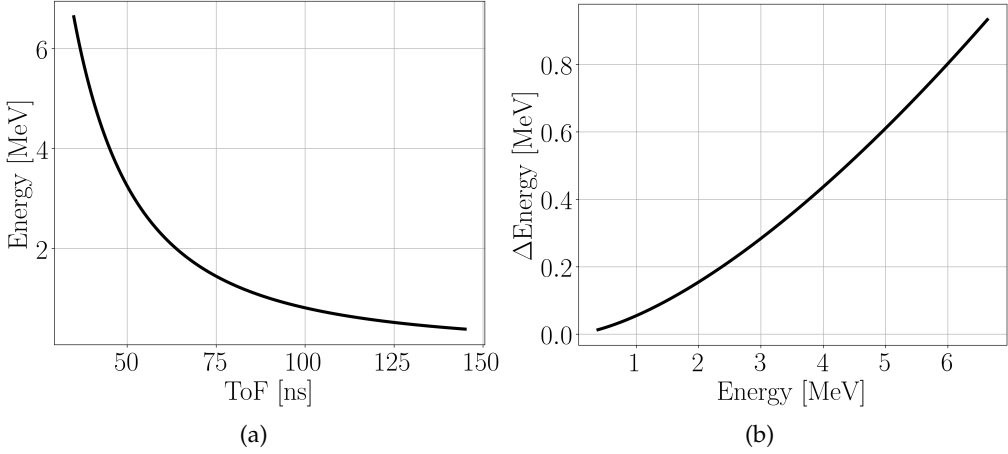


Figure 28: (a) Mapping from ToF to neutron energy:  $E = \frac{8127}{T_0 F^2}$ . (b) Uncertainty in neutron energy measurements as a function of measured neutron energy.

relative to the center of a scintillator, the difference between the times of signals from the two PMTs,  $\Delta t^{PMTs}$ , is given by:

$$\begin{aligned} \Delta t^{PMTs} &= t^{PMT_1} - t^{PMT_2} \\ &= \frac{(L/2 + x)n_{\text{eff}}}{c} - \frac{(L/2 - x)n_{\text{eff}}}{c} \\ &= 2x \frac{n_{\text{eff}}}{c}. \end{aligned} \quad (2.1)$$

Solving for  $x$  gives

$$x = \frac{c}{2n_{\text{eff}}} \Delta t^{PMTs} \quad (2.2)$$

where  $t^{PMT_{top}}$  and  $t^{PMT_{bot}}$  are the times of signals from the top and bottom PMTs of a detector,  $L$  is the length of the scintillator,  $c$  is the speed of light,  $n_{\text{eff}}$  is the effective index of refraction of the scintillator. Using data taken from coincident photons from a collimated  $^{60}\text{Co}$  placed at different position on a detector, a least squares linear fit between  $x$  and  $\Delta t^{PMTs}$  was performed. The resulting fit parameters are used to find the position of detected particles.

The slope of the linear fit in Fig. 29(a), along with Eq. 2.2, can be used to cal-

## 2. METHODS

---

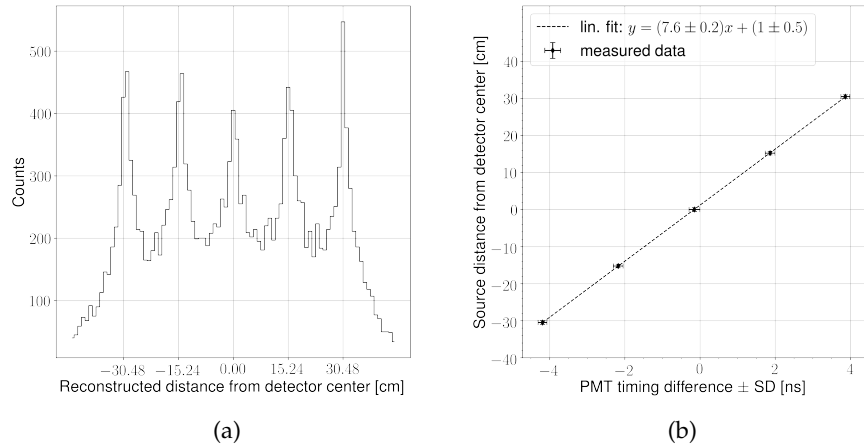


Figure 29: A collimated  $^{60}\text{Co}$  source is used to produce photon events at five different positions along the scintillator with a spot size of less than 1 cm. Aggregating the data produces the five peaks seen in (a). The  $\pm 9$  cm width of each of these peaks is due to uncertainty in the measurement of particle position. As seen in (b), the mean PMT timing difference of events at each position varies linearly with respect to the distance of the  $^{60}\text{Co}$  from the center of the detector. The result of a linear least squares fit to this data is used to calculate the position of detected particles.

culate the effective index of refraction, giving a value of 2.0 . The index of refraction measured here is said to be “effective” because its measurement is sensitive to scintillation light’s speed only along the axis parallel to the scintillator’s longest dimension, and because scintillation light does not necessarily take a straight path to the PMTs, this speed is not equal to the intrinsic speed of light in the material. The actual index of refraction of PVT is known to be 1.58, or  $\sim 20\%$  less than the value measured here, indicating that there is some reflection of detected scintillation light from the boundaries of the scintillator. This effect contributes to the width of the peaks in Fig. 29(b).

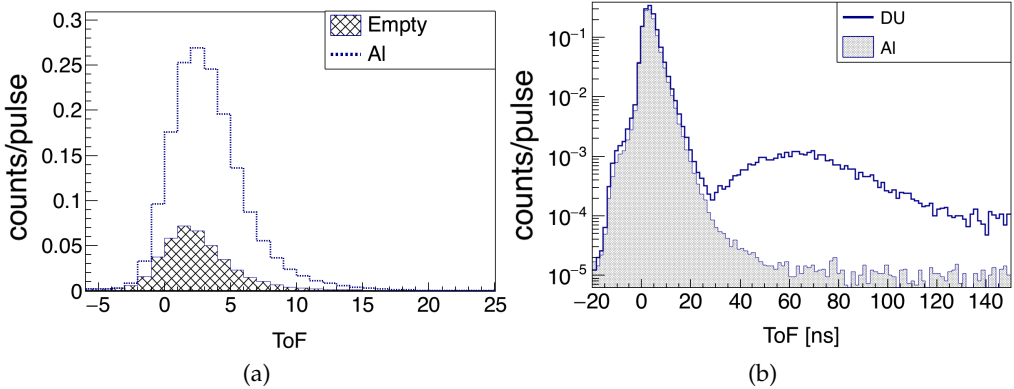


Figure 210: (a) Comparison between the ToF spectrum of a non-neutron producing target made from Al, to the ToF spectrum produced when no target is used. The large increase in events around 4 ns is due to photons that scatter from the Al target. When no target is in place, sources of the peak include: the collimator leading into the experimental cell, and the beam dump. The photon peak seen here is used to find the timing offsets that make it so  $t = 0$  corresponds to the moment of fission. (b) Comparison between the Al and DU targets show a pronounced increase in events between 35 and 130 ns due to the introduction of neutrons.

### 2.2.3 DU Target

A depleted uranium (DU) target with dimensions of  $4 \times 2 \times 0.05 \text{ cm}^3$  was used as the primary target. DU received the majority of the allotted beam time because it is an even-even nucleus, and as a consequence, the fission fragments are emitted with a high degree of anisotropy [?]. Because the target lacked cylindrical symmetry, it was rotated slowly about the vertical axis during the experiment. This was done in order to remove the potential for bias due to the elastic scattering of neutrons within the target. See section 3.2.2 for details.

### 2.2.4 Electronics

A data acquisition system based on NIM/VME standard was used. A schematic of the data acquisition logic is shown in Figure 211. The PMTs are supplied voltages ranging from 1300 to 1500 V by a LeCroy 1458 high voltage mainframe.

## 2. METHODS

---

Analog signals from the PMTs were fed into a leading edge discriminator with input thresholds ranging from 30 mV to 50 mV. The logic signals from the discriminator were then converted to ECL logic and fed into a CAEN model V1290A TDC. The timing of signals from the PMTs were always measured relative to a signal from the accelerator provided at the beginning of each pulse. Only the first signal from a given PMT each pulse is accepted. On the software side, the CODA software package developed by Jefferson Laboratory [?] was used to carry out the acquisition of data from the TDC and convert it into a usable format.

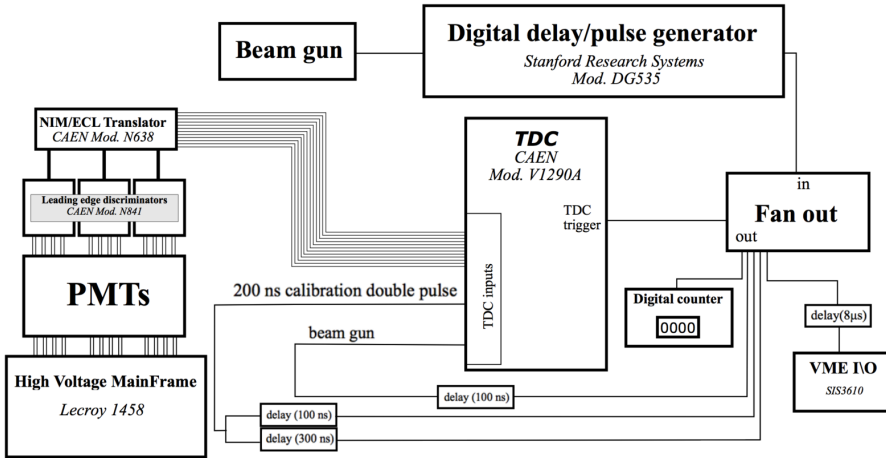


Figure 211: Wiring diagram of the electronics setup.

### Detector Shielding

The detector's shielding was designed with the aim of reducing cross-talk, the detection of photons, and noise. The front face of the detectors, facing towards the target, were subject to the highest gammas flux due to the scattering of the beam from the target. The detection of a gamma renders a detector "dead" during the time at which subsequent fission neutrons from the same pulse reach the detector. Lead can mitigate this problem by attenuating gammas,

but has the side effect of scattering neutrons. If a neutron scatters prior to being detected, the ToF calculation will be incorrect because the neutron traveled an unknown distance to the detector. The extent that neutron travel distances are perturbed due to scattering from lead shielding was quantified using an MCNP . Accordingly, 1" of lead was placed along the front face of the detectors. This diminished gamma detection rates to reasonable levels and, according to the simulation, caused a negligible amount of neutron scattering. Because of particularly high gamma flux, an additional 2" of lead was placed at the sides of detectors adjacent to the beam, and along the front faces of the detectors farthest downstream at  $\pm 30^\circ$  from the beam line. Placing lead behind the detectors was avoided in consideration of an MCNP-POLIMI simulation, which indicated that lead placed here facilitates cross-talk. Because cross-talk events are in fact correlated, they cannot be removed in analysis by the subtraction of accidentals. For more information about cross-talk, see section 3.2.

### 2.2.5 Measurements with $^{252}\text{Cf}$

Opening angle measurements were also performed on neutrons from the spontaneous fission (SF) of  $^{252}\text{Cf}$ . Several such past measurements have been performed, and so they serve as a means to validate the methods used in this study.

As opposed to the measurements of neutrons from photofission, there is no concern over the detection of accidental neutron coincidences, because given the strength of the  $^{252}\text{Cf}$  source, it is highly unlikely that two fissions occur during the acceptance time window of 150 ns. Another difference between the two measurements is the clean and sharp peak produced by fission photons from  $^{252}\text{Cf}$  compared to a relatively smeared peak produced by photons scat-

## 2. METHODS

---

tering from the target during measurements of photo-neutrons. In each measurement, the photon peak is used as a reference point for the calculation of neutron ToF. As a result the  $^{252}\text{Cf}$  measurements have less error in ToF caused by the spreading of the photon peak. The same normalization technique is used for both SF and photon-neutron measurements, in which the correlated distribution is divided by the uncorrelated distribution of neutron pairs taken from different fissions.

Instead of using the beam for a trigger, the trigger for  $^{252}\text{Cf}$  consisted of two high timing-resolution scintillation detectors made from ATP plastic, in which one is fixed below and the other above the source at a distance of 15 cm. Using a coincidence window of 4 ns, which is intended to select for coincident photons from fission, the trigger required 2-fold coincidence between both of the scintillation detectors.

### 2.3 Analysis

#### 2.3.1 Cancelation of Detector Efficiencies, Drifts, and Geometric Phase Space

The efficiency and acceptance of the neutron detection system varies greatly over its opening angle range from  $20^\circ$  to  $180^\circ$ , as illustrated in Fig. 212(a). This is both due to the neutron detection system's non-spherical symmetry and to varying efficiency as a function of particle position on the detector. In order to give a result that is sensitive to angular correlations but insensitive to detector efficiencies and experimental drifts, angular correlation is always calculated by

the following fraction:

$$\text{angular correlation} \propto \frac{nn_{\text{corr}}(\theta)}{nn_{\text{uncorr}}(\theta)},$$

where  $nn_{\text{uncorr}}(\theta)$ <sup>1</sup> is produced from a manufactured set of opening angles, hereafter denoted by  $nn_{DP}(\theta)$ , by pairing neutron events that occurred during different pulses, and  $nn_{\text{corr}}(\theta)$  is the accidental subtracted opening angle distribution, which is described in section 2.3.2.

$nn_{DP}(\theta)$  is constructed by examining pulses in pairs of two, which are required to have occurred within 0.2 seconds of each other, and for those pairs that have an event in both pulses, the opening angle is calculated between the events in the same way that it would be for coincident events from the same pulse.  $nn_{\text{uncorr}}(\theta)$  is a subset of  $nn_{DP}(\theta)$  which only uses pulse pairs that have two neutron events in both pulses, and, as a result, four pairs of uncorrelated neutrons can be formed from each pulse pair used in  $nn_{\text{uncorr}}$ . The reason for doing this is to increase the percentage of pairs of fission neutrons in  $nn_{\text{uncorr}}(\theta)$ , as opposed to pairs of neutrons from  $(\gamma, n)$ . This is an important point because the detection of multiple neutrons from  $(\gamma, n)$  are completely removed from  $nn_{\text{corr}}(\theta)$  (the numerator in  $\frac{nn_{\text{corr}}(\theta)}{nn_{\text{uncorr}}(\theta)}$ ) due to the subtraction of accidental coincidences.

As long as the numerator and denominator are comprised of neutron pairs with the same energies, the ratio between  $nn_{\text{corr}}(\theta)$  and  $nn_{\text{uncorr}}$  does not depend on detector efficiency. Thus, because the two energy distributions are not necessarily the same, the following calculation gives a result that is integrated over some set,  $C$ , of neutron-neutron energies (also referred to as an *energy*

---

<sup>1</sup>While this notation implies that coincident events are only due to neutrons, about 3% of total  $nn_{\text{corr}}(\theta)$  events are not due to neutrons. This was determined by comparing data from a non-neutron producing Al target to that from a  $^{238}\text{U}$  target (see Fig. 214)

## 2. METHODS

---

*cut*):

$$\text{integrated angular correlation} \propto \iint_{(E_1, E_2) \in C} \frac{nn_{\text{corr}}(\theta_{nn}, E_1, E_2)}{nn_{\text{uncorr}}(\theta_{nn}, E_1, E_2)} dE_1 dE_2 \quad (2.3)$$

Because Eq. 2.3 exhibits no dependence on experimental parameters, the same quantity can be calculated from the output of a model such as FREYA and compared by side-by-side with measurements.

Figure 212(a) shows the measured  $nn_{\text{corr}}(\theta)$  yield distribution of neutrons from the photofission of  $^{238}\text{U}$ . The structure seen here is reflective of the underlying two-neutron angular correlations as well as the geometric acceptance and efficiencies of the neutron detectors. Figure 212(b) reveals how a clear picture of two-neutron correlations emerges when taking the ratio between  $nn_{\text{corr}}(\theta)$  and  $nn_{\text{uncorr}}(\theta)$ .

The photo-disintegration of  $\text{D}_2\text{O}$ , which produces uncorrelated neutrons, gives a flat distribution in  $\cos(\theta_{nn})$ , as expected (see Fig. 213).

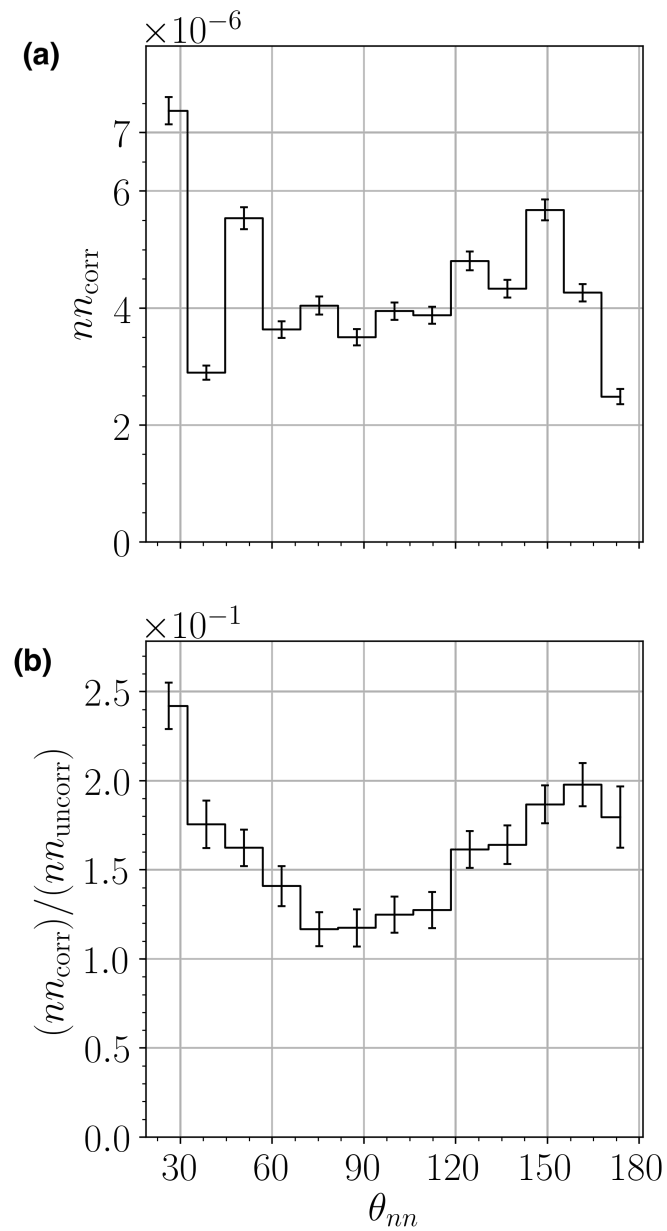


Figure 212: (a) Two-neutron opening angle distribution from the photofission of  $^{238}\text{U}$  before normalization, and, (b) after normalizing to the distribution of uncorrelated two-neutron events from different pulses. All measured neutrons have an energy greater than 0.4 MeV.

## 2. METHODS

---

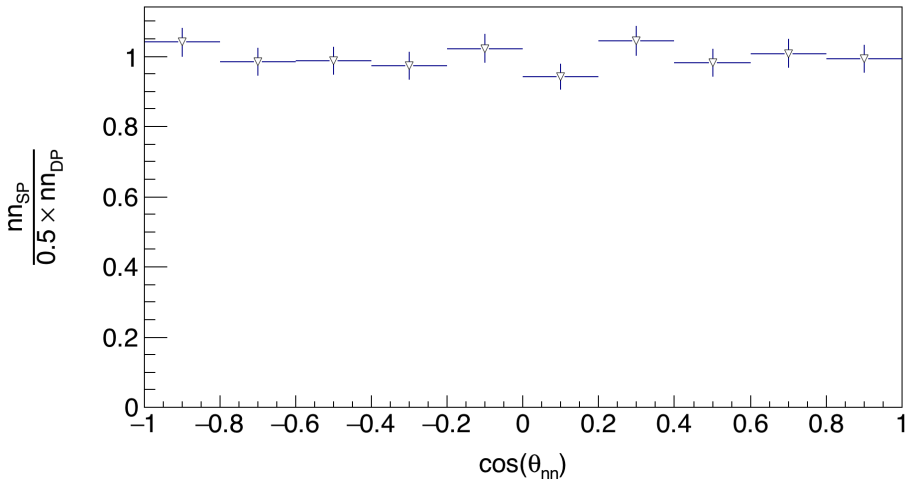


Figure 213: The opening angle distribution of neutrons from the photo-disintegration of D<sub>2</sub>O is uniform in  $\cos(\theta)$ , or in otherwise isotropic, as expected.  $nn_{SP}$  and  $nn_{DP}$  are the relative yields of neutron formed from the neutron events from the same pulse and from different pulses, respectively.

### 2.3.2 Subtraction of Accidental Coincidences

The detection of two uncorrelated events in coincidence, whether caused by neutrons, photons, or noise, is referred to as an *accidental*. A small number of accidental photon events will exist in the neutron time of flight range because of the smearing of the photon peak. These events are accidentals, because they are extremely likely to be due to photons from the beam, and not photons from fission. There are also accidentals due to noise, which can be estimated with a non-neutron producing target made from aluminum (see Fig. 214). The accelerator's current was adjusted so that there are, on average, less than 1.0 fissions per pulse, but nevertheless statistical fluctuations in the number of fissions per pulse result in accidental coincident neutrons that originated from different, and therefore, uncorrelated fissions. There are also uncorrelated neutrons produced when multiple ( $\gamma, n$ ) reactions occur in a single pulse. The <sup>238</sup>U cross-section of ( $\gamma, n$ ), integrated over the relevant bremsstrahlung energy distribution, is about a factor of 5 times greater than it is for photofission

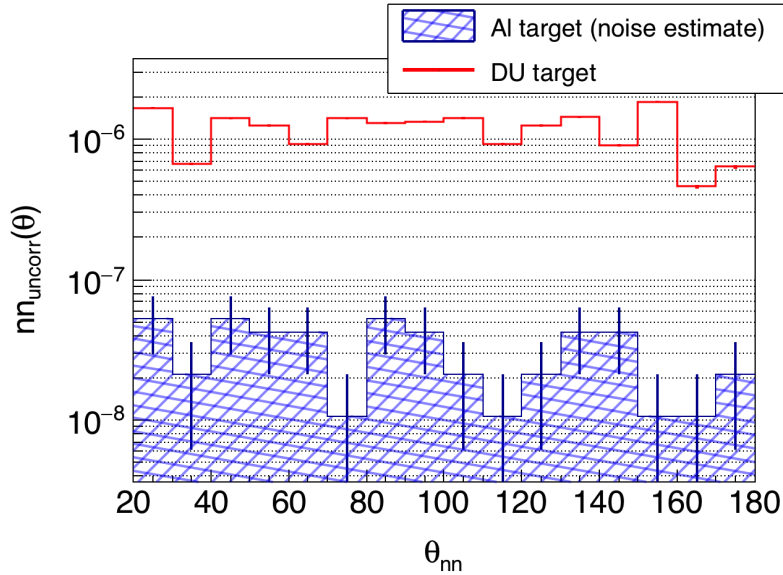


Figure 214: An Al target was designed to scatter the same number of photons as the DU target, thus serving as an equivalent non-neutron producing target well-suited to estimate noise. The rate of coincident events for the Al target is 3% that of the DU target.

(see Fig. 215). As a result, it is unavoidable that there be a significant number of neutron coincidences caused by multiple  $(\gamma, n)$  reactions relative to those caused by correlated fission neutrons. If not subtracted from the result, the opening angle distribution of uncorrelated neutrons will wash out the signal from correlated neutrons.

The raw measurement consists of a mix of correlated and accidental neutron coincidences, that is

$$nn_{\text{raw}}(\theta) = nn_{\text{corr}}(\theta) + nn_{\text{acc}}(\theta) \quad (2.4)$$

where  $nn_{\text{raw}}(\theta)$  and  $nn_{\text{acc}}(\theta)$  are the rates, per pulse, of the detection of neutron pairs with opening angle of  $\theta$  for all events and for accidental coincident events, respectively.

Because accidental coincidences consist of two independent events, it does not

## 2. METHODS

---

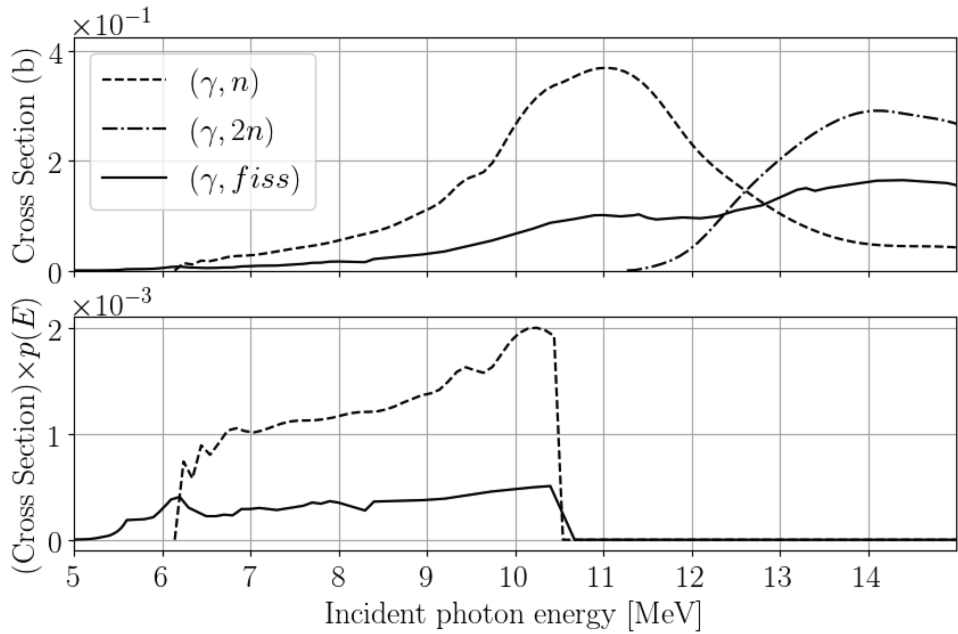


Figure 215: (top) ENDF cross-sections of  $(\gamma, \text{fiss})$  and direct  $(\gamma, n)$  and direct  $(\gamma, 2n)$ . (bottom) Cross-sections integrated over the simulated relative rate of bremsstrahlung photons that reach the target as a function of photon energy. The integrated cross-sections of  $(\gamma, n)$  is 5.5 times greater than for  $(\gamma, \text{fiss})$ .

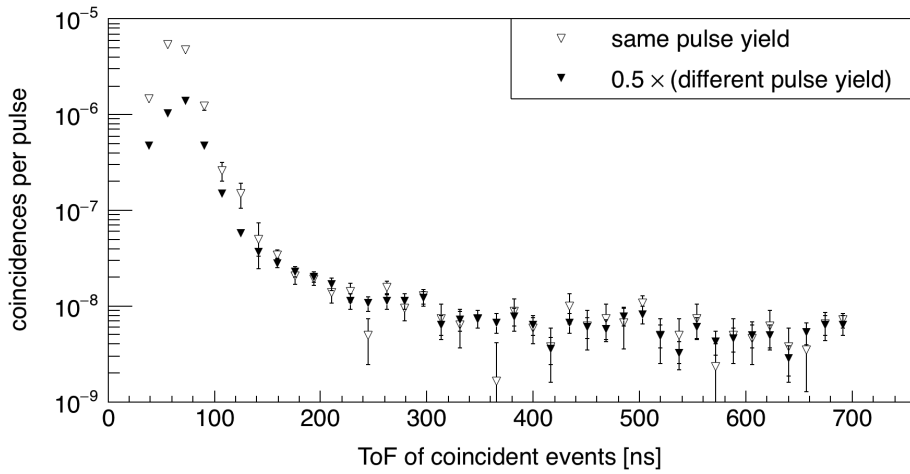


Figure 216: The different pulse yield captures the effects of noise due to accidentals. The y-axis represents the number of coincidences in which both events had a ToF within a given 20 ns wide bin. Because events with a ToF above 120 ns are predominately due to noise, which correspond to a 0.5 MeV neutron, the same pulse yield is equal to 1/2 times the different pulse yield.

matter whether the two events occurred during the same pulse or during two different pulses, given that the two different pulses occurred at around the same time and thus under the same experimental conditions. Thus,  $nn_{DP}(\theta)$  is proportional to  $nn_{acc}(\theta)$ , in other words, the two distribution have opening angle distributions with the same shape. However,  $nn_{acc}(\theta)$  is not equal to  $nn_{DP}(\theta)$ , because there are, on average, twice as many events in a pulse-pair than there are in a single pulse. For this reason, as the following analysis shows,  $nn_{acc}(\theta) = \frac{1}{2}nn_{DP}(\theta)$ .

The number of uncorrelated events detected per pulse is assumed to follow the Poissonian distribution, which describes the occurrence of independent random events. Let  $\lambda$  represent the mean number of uncorrelated events per pulse. To determine the value of  $\lambda$ , one needs to know whether a given coincident event is in fact an accidental, as  $\lambda$  only quantifies the rate of accidental coincidences. Such information is not known, but the largest possible value for  $\lambda$  is the mean number of events per pulse, because this assumes all events are uncorrelated. This places an upper bound on  $\lambda$  of  $3 \times 10^{-6}$  for this work, which is small enough to neglect all terms on the order of  $\lambda^3$  or greater.

The per-pulse accidental coincidence rate of individual pulses summed over all opening angle bins, denoted by  $\sum_\theta nn_{acc}(\theta)$ , is equal to the poissonian probability of there being exactly two events detected in a single pulse<sup>2</sup>:

$$\begin{aligned}\sum_\theta nn_{acc}(\theta) &= \frac{e^{-\lambda}\lambda^2}{2!} \\ &\approx \frac{\lambda^2}{2} + \mathcal{O}(\lambda^3).\end{aligned}\tag{2.5}$$

---

<sup>2</sup>For the sake of brevity, cases of greater than two-fold coincidence are not considered in this analysis, and it is not necessary because of the low detection rates during this work. It can be shown, however, that accounting for any number of coincidences, from zero all the way up to  $\infty$ -fold coincident events in a pulse or pulse-pair, will give the same answer.

## 2. METHODS

---

For the case of different-pulse pairs, a “coincidence” occurs when there is an event in both pulses. Cases in which there are more than two events can be neglected due to their rare occurrence in this work, therefore, the per-pulse rate for different-pulse pairs, again summed over all opening angle bins, is the square of the poissonian probability of there being one event:

$$\sum_{\theta} nn_{DP}(\theta) = \left( e^{-\lambda} \lambda \right)^2 \approx \lambda^2 + \mathcal{O}(\lambda^3). \quad (2.6)$$

For the reasons explained above,  $nn_{DP}(\theta)$  and  $nn_{acc}(\theta)$  have the same shape, thus, from Eq.’s (2.6) and (2.5) it follows that

$$nn_{acc}(\theta) = \frac{1}{2} nn_{DP}(\theta). \quad (2.7)$$

## Chapter 3

---

# Discussion of Experimental Errors

---

## 3.1 Random Errors

### 3.1.1 Resolution of measurement

The position of a detected particle is known to within a specified distance, which translates into a resolution in the measurement of the opening angle between a pair of particles. A particle's reconstructed position along a detector's length has an error of  $\pm 13$  cm. Due to the detector's 15 cm width, there is also a positional uncertainty of  $\pm 7.5$  cm in the direction perpendicular to the detector's length. The amount of uncertainty in a single two-neutron opening angle measurement is determined from the uncertainties in the positions of each detected neutron. These positional uncertainties are propagated through the formula for the calculation of opening angle, which is

$$\theta_{nn} = \arccos \left( \frac{\vec{v}_1 \cdot \vec{v}_2}{|\vec{v}_1| |\vec{v}_2|} \right)$$

where  $\vec{v}_1 = (x_1, y_1, z_1)$  and  $\vec{v}_2 = (x_2, y_2, z_2)$  are the detected positions of the two neutrons. The propagation of error through this formula is achieved by

### 3. DISCUSSION OF EXPERIMENTAL ERRORS

---

evaluating the following expression

$$\Delta\theta_{nn} = \left( \left( \Delta x_1 \frac{\partial\theta}{\partial x_1} \right)^2 + \left( \Delta y_1 \frac{\partial\theta}{\partial y_1} \right)^2 + \left( \Delta z_1 \frac{\partial\theta}{\partial z_1} \right)^2 + \left( \Delta x_2 \frac{\partial\theta}{\partial x_2} \right)^2 + \left( \Delta y_2 \frac{\partial\theta}{\partial y_2} \right)^2 + \left( \Delta z_2 \frac{\partial\theta}{\partial z_2} \right)^2 \right)^{\frac{1}{2}}$$

, where the  $\Delta$ 's represent the uncertainty in the variable that directly follows each  $\Delta$ . The values and uncertainties of all events in a given angle bin are fed through Eq.3.1, and then averaged together. The result, seen in Fig. 31, can be interpreted as the opening angle resolution as a function of  $\theta$ .

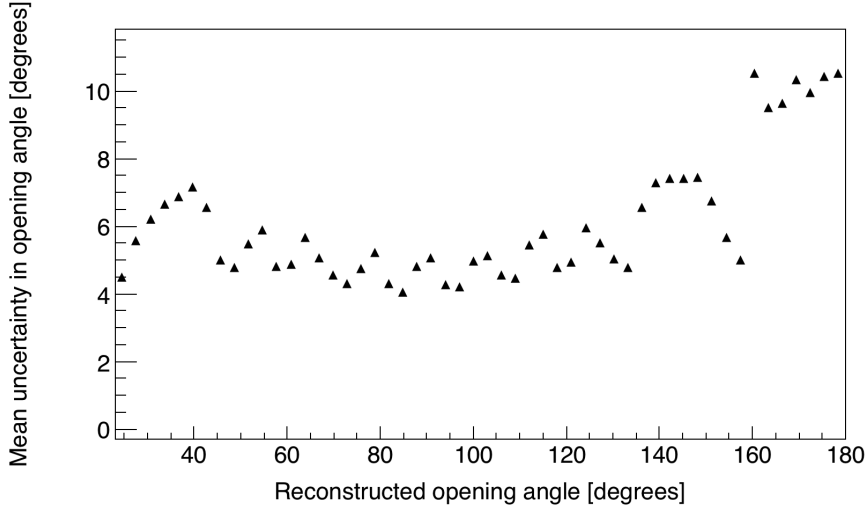


Figure 31: Uncertainties in opening angle determined from the propagation of position uncertainties through the opening angle calculation. The uncertainty of a given opening angle measurement depends on which detectors are involved and the position of the particles on the detectors. For this reason, the uncertainty of measurements falling within each angle bin is a distribution, so the average uncertainties are plotted here. The y-axis can be viewed as a measure of angular resolution in the sense that it represents the smallest angular difference that can be considered statistically significant.

### 3.1.2 Counting error

The uncertainty in the number of observed events is always assumed to be equal to  $\sqrt{N}$ , as per poissonian statistics, where N is the number of observed events. This value is then propagated through all the analysis procedure using the standard methods for the propagation of error. The vertical error bars seen in all results are due solely to such counting error.

## 3.2 Detector Cross-talk

*Cross-talk* occurs when, after a particle is detected once, the same particle, by any means, causes a detection to be registered in a different detector. For example, upon detection, a particle may undergo elastic scattering and then travel into another detector where it is detected again, or it may produce secondary particles that are detected. The two coincident detections of a cross-talk event are causally correlated, and thus they have the potential to contaminate the signal from correlated fission neutrons. If both detections occur during the ToF range typical for fission neutrons, then the cross-talk event cannot be distinguished from the detection of two correlated neutrons.

Recent works that measured the two-neutron angular correlations in the spontaneous fission of  $^{252}\text{Cf}$  and  $^{240}\text{Pu}$  [?, ?] addressed this effect by using an MCNP-PoLiMi simulation to estimate and then subtract cross-talk from their measurements. In this work, the issue of cross-talk is approached differently by employing the use of detector shielding aimed at reducing cross-talk to a negligible rate. By using shielding to reduce cross-talk, this measurement is less dependent on the details of the models used by MCNP-PoLiMi to simulate neutron transport and detection. MCNP-PoLoMi simulations are used in this work

### 3. DISCUSSION OF EXPERIMENTAL ERRORS

---

only to verify that the effect of cross-talk is negligible. The scintillators used here are much larger than those used in similar works, such as in refs [?, ?], allowing for them to be placed much farther from the fission source without causing extremely low coincidence rates. An increase in the distance between the detectors and the fission source makes this measurement less sensitive to angular uncertainty, which is influenced by the uncertainty in the position of a detected particle, due to, for example, the scattering of neutrons from detector shielding. Because of this, larger amounts of shielding can be used without concern of introducing large errors.

The geometry of the neutron detection system makes it kinematically impossible for a neutron to scatter from a proton in one detector—which is the basis for scintillation—and then travel directly into another detector with enough kinetic energy to be detected a second time. For this reason, upon being detected, a neutron must scatter from one or more intermediate nuclei, such as Pb or C, in order for it to reach a different detector with enough energy to be detected a second time. This fact follows from the conservation of energy and momentum. Figure 32 illustrates a cross-talk event due to a neutron scattering in a detector’s shielding. In order to be more convinced that such events occur at negligible rates, a detailed MCNP-PoliMi [?] simulation was performed to model cross-talk.

#### 3.2.1 Cross-talk Simulation

The simulation included all scintillators and their shielding, supporting structures, and the concrete walls surrounding the experimental cell. MCNP-PoliMi’s built-in  $^{252}\text{Cf}$  spontaneous fission source was used, which emits neutrons with the correct correlations and multiplicities. Detector response was modeled us-

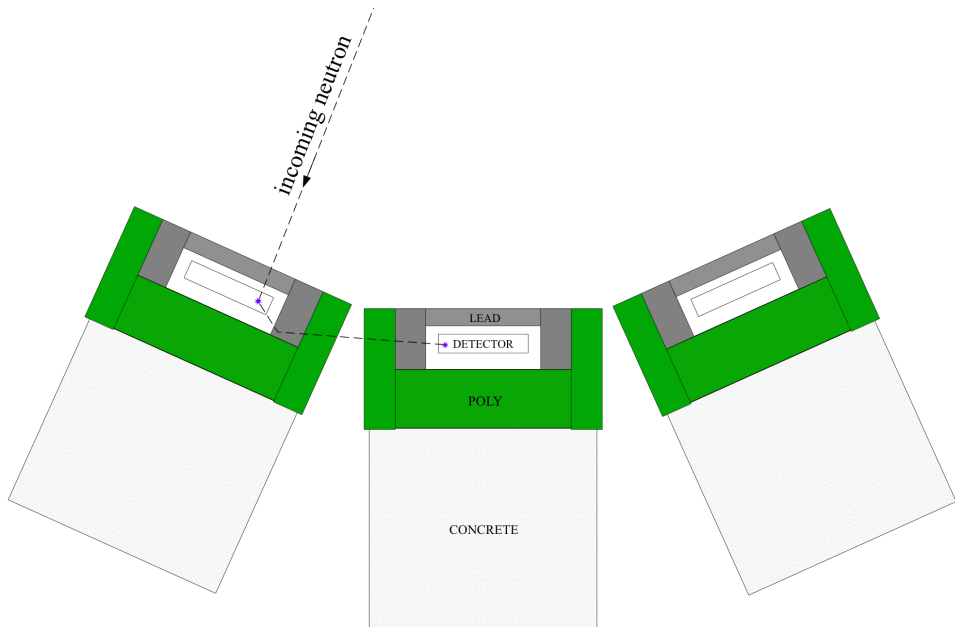


Figure 32: A hypothetical example of a neutron cross-talk event. An incoming neutron detected and then scatters from some lead shielding nearby, which changes its direction of travel such that it enters a second detector where it is detected a second time. The scattering of a neutron from an intermediate nucleus, in this example a lead nucleus, is kinematically required in order for cross-talk to occur in this experiment.

ing a program included with the MCNP-PoliMi distribution called MPPost [?]. The model is based on the electron equivalent light output (MeVee) produced by particles as they undergo collisions with carbon and hydrogen within organic plastic scintillators. A minimum deposited energy of 0.4 MeV (0.05 MeVee for neutrons) was assumed for detectable particles, which was chosen because the neutron detection system showed a sharp decline in detection rates for neutrons below 0.4 MeV. For neutron collisions with hydrogen, the light output in MeVee,  $L$ , is calculated by the following empirically derived formula

$$L = 0.0364E_n^2 + 0.125E_n$$

### 3. DISCUSSION OF EXPERIMENTAL ERRORS

---

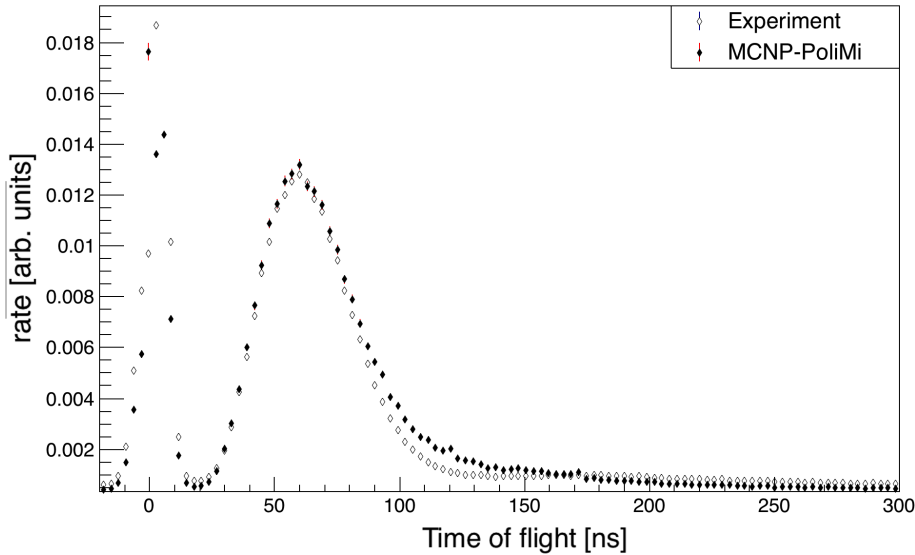


Figure 33: Measured vs simulated ToF spectrum of a  $^{252}\text{Cf}$  spontaneous fission source. The simulation also used a detector response model based on ref [?]

where  $E_n$  is equal to the loss in the kinetic energy of the neutron due to the collision. Neutron interactions with carbon are assumed to generate a small light output of

$$L = 0.02E_n$$

As seen in Fig. 33, this model produces a ToF spectrum that is in good agreement with the measurement.

The simulation was initially performed with 5 cm of lead shielding placed behind the scintillators, and the number of cross-talk events accounted for 11% of the total coincident neutron events. The amount of cross-talk fell to 3% if polyethylene was used instead of lead, which motivated the placement of 5 cm of polyethylene behind the detectors during construction. Figure 34 shows the distribution of cross-talk events and true two-neutron coincidences as a function of reconstructed opening angle. It is worth noting that, according to the simulation, the effect of cross-talk is not only small, but is also distributed over a wide range of angles rather than being concentrated around  $\theta_{nn} = 0$ .

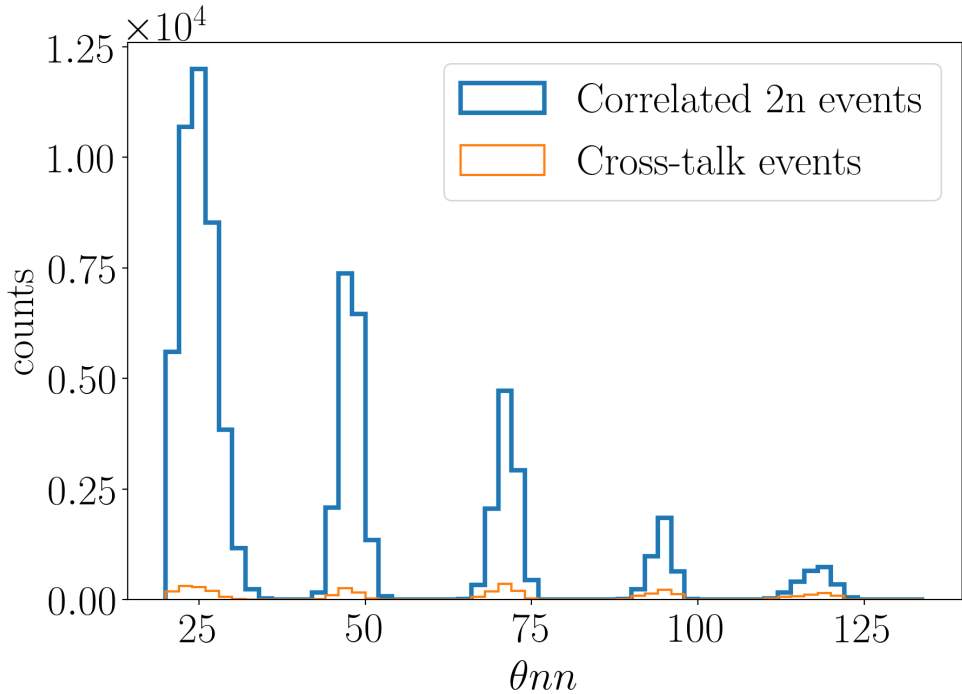


Figure 34: MCNP-PoLiMi simulation of the number of cross-talk events versus correlated two-neutron events as a function of reconstructed opening angle. Cross-talk accounted for 3% of total events. In this work, cross-talk does not occur primarily at small angles, but is instead spread out over a wide range of angles.

Angles greater than 125 degrees are not shown in Fig. 34, because these cross-talk events can be readily identified in analysis by the large amount of time required for a neutron to travel the required distances.

### 3.2.2 Neutron Scattering within Target

A potential source of error in opening angle measurements is the scattering of neutrons within the fission target. This is a cause for concern, because a neutron that scatters from a heavy nuclei is very likely to be deflected at a large angle, creating two-neutron opening angles that are not reflective of the true opening angle immediately after fission. Furthermore, because the target used in this work has the shape of a thin strip, it is more likely that neutrons that

### 3. DISCUSSION OF EXPERIMENTAL ERRORS

---

are initially traveling towards a given detector are deflected away by scattering if said detector is aligned along the wide (2 cm) axis of the strip, as opposed to the thin (0.05 cm) axis. This bias is removed by slowly rotating the target about the vertical axis during data acquisition. Because the subject of this measurement is fundamentally a statistical process, useful interpretations of the data are average rates taken over many events. Thus, by rotating the target, cylindrical symmetry is preserved in the average, producing a result equivalent to that if a cylindrical target were used.

A thin strip is the ideal target shape regarding the rate of neutron elastic scattering per unit volume. See Fig 35 for the result of an MCNP simulation of the elastic scattering rates for both thin strip and cylindrical shaped targets. The target in this experiment was a thin strip with a width 40 times greater than its thickness, for which the simulation indicated the rate of elastic scattering is roughly a factor of two less than for a cylindrical target of the same volume.

The target's dimensions are small enough that the rate of photon absorption, and thus photo-neutron production, is virtually uniform throughout the entire target volume. MCNP was used to simulate the production of pairs of fission neutrons uniformly throughout the target volume with energies typical of fission neutrons. The probability that at least one neutron out of a pair of two scatters before exiting the target was calculated from the simulation. For the target used in this work, the simulation indicated that 6% of two-neutron opening angles were altered due to scattering.

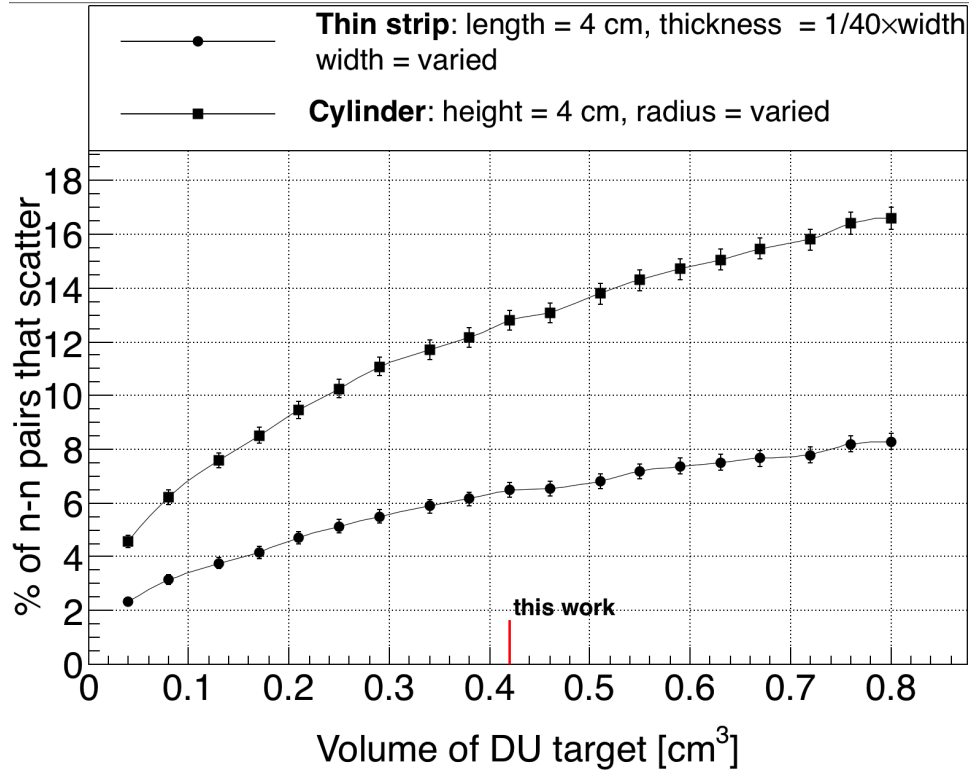


Figure 35: Result of an MCNP simulation in which neutron-neutron pairs, with energies sampled from a typical watt fission spectrum, were generated uniformly throughout the volume of DU targets. The y-axis is the rate of opening angle contamination due to the scattering of, within the DU target in which they were produced, either one or both of a pair of neutrons. The lack of symmetry of a thin strip target can be removed by slowly rotating the target around the vertical axis during data acquisition, making it the optimal target geometry for the minimization of the rate of neutron scattering. The target used in this work had a length of 4 cm, a width of 2 cm, and a thickness of 0.05 cm.



## Chapter 4

---

# Results

---

### 4.1 Asymmetries in $\theta_{abs}$ of Neutron Singles

Using data acquired during this study, it is possible to construct  $\theta_{abs}$  distributions of neutron singles, where  $\theta_{abs}$  is defined as the angle between a neutron's reconstructed direction of travel and the direction of the incident photon beam. Because the experimental design was motivated by measurements of correlated neutron doubles and not neutron singles, the methods required to obtain a neutron singles measurement are far less robust than for neutron doubles. Nonetheless, neutron singles measurements from the photo-disintegration of D<sub>2</sub>O showed fair agreement with known values, so these results are not totally without merit.

The distributions were calculated by normalizing a yield of photo-neutrons to the yield of neutrons from SF of <sup>252</sup>Cf, which have no preferred direction. However, these two yields were measured under very different experimental conditions. This is different from the case of two-neutron opening angle measurements, which uses the same set of neutron events to generate two yields—uncorrected yield and correlated yield. Another difference for these measurements is that there is no uncorrelated yield to use to subtract undesir-

#### 4. RESULTS

---

able signals from noise and photons.

Due to differences in experimental conditions that existed during measurements of photo-neutrons and measurements of neutrons from the SF of  $^{252}\text{Cf}$ , there is a high potential for systematic errors. The photo-neutron data must be corrected for detector dead-time, which, due to the presence of the photon beam, was about an order of magnitude higher for photo-neutron measurements than for  $^{252}\text{Cf}$  measurements. Accidental coincidences caused by noise and photons was estimated from data taken with a non-neutron producing aluminum target, which had to also be corrected for dead-time, and, scaled to account for the fact that the aluminum and photo-neutron data sets have different gamma detection rates. The result was then subtracted from the photo-neutron data. Neutrons from the SF of  $^{252}\text{Cf}$  do not have the same energy distribution as photo-neutrons, which could lead to incorrect results.

Despite all this, the  $\theta_{abs}$  distribution for  $\text{D}_2\text{O}$  agrees moderately well with the previously established distribution, but the same may not necessarily be true for  $^{238}\text{U}$  and  $^{232}\text{Th}$ , which have a signal-to-noise ratio that is about 7 and 100 times less than for  $\text{D}_2\text{O}$ , respectively.

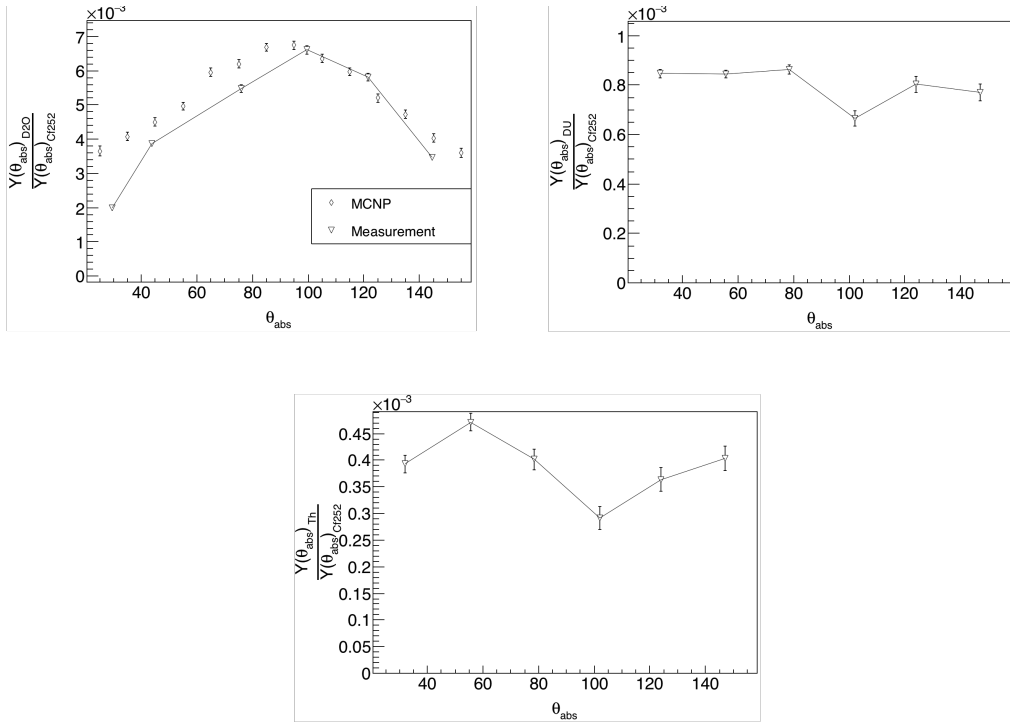


Figure 41: Accessory calculations were performed of the relative rates of neutrons singles as a function of  $\theta_{abs}$ . Results are expressed as a ratio of the yield of photo-neutron singles from  $D_2O$ ,  $^{238}U$  (DU), and  $^{232}Th$ , to the yield of neutron singles from the SF of  $^{252}Cf$ . The result for  $D_2O$  is in fair agreement with past measurements, however, these results have high potential for systematic errors due to the differences in experimental conditions under which the yields in the numerator and denominator (of the label for the y-axis) were measured.

## 4.2 Two-neutron opening Angle Correlations

Two-neutron opening angle correlation is calculated using the methods outlined in sec 2.3, in which a correlated neutron yield is divided by an uncorrelated yield. The results are compared with output from FREYA [?] (Fission Reaction Event Yield Algorithm), which was developed by the collaborative efforts of researchers from Lawrence Berkeley National Laboratory, Lawrence Livermore National Laboratory, Los Alamos National Laboratory, and University of Michigan Nuclear Engineering, and has been included in MCNP beginning with version 6.2 .

#### 4. RESULTS

---

The most recent release of FREYA (version 2.0.3) does not model photofission directly, but instead uses a neutron-induced fission model to approximate photofission [?]. For a given nucleus with  $Z$  protons and  $A$  total nucleons, the code selects the neutron-induced fission model for a  $Z(A-1)$  nucleus, and chooses an incident neutron energy such that the compound  $ZA$  nucleus will have an excitation energy relative to the ground state of  $ZA$  that is equal to the energy of the incident photon. All model parameters, such as level density and partition parameters, were set to their default values for neutron-induced fission. FREYA was told to use the fission fragment mass distribution,  $Y(A)$ , and the average total kinetic energy,  $\langle TKE \rangle(A)$ , from the  $^{238}\text{U}$  photofission measurements described in ref [?].

In ref [?], the authors warn that using FREYA in this way to model photofission is only an approximation and could lead to incorrect results. Nonetheless, FREYA is used here as such because it is the only photofission model available to the authors of the present work.

The measured  $\theta_{nn}$  distribution from the photofission of  $^{238}\text{U}$  and the SF of  $^{252}\text{Cf}$  are presented with the following three different types of cuts applied to the energies of neutrons in coincidence:

- (i) In Figs. 43 ( $^{238}\text{U}$ ) and 46 ( $^{252}\text{Cf}$ ), a minimum energy threshold is applied to both neutrons,
- (ii) In Figs. 44 ( $^{238}\text{U}$ ) and 47 ( $^{252}\text{Cf}$ ), the mean energy of the two neutrons are required to fall within a specified range.
- (iii) In Figs. 42 ( $^{238}\text{U}$ ) and 45 ( $^{252}\text{Cf}$ ), the energy of both neutrons are required to fall within a specified range.

When using a histogram to estimate a continuous distribution from the rela-

tively small number of data points obtained of neutrons from the photofission of  $^{238}\text{U}$ , one faces the following dilemma: small bins produce histograms with large uncertainties that are dependent on the chosen bin-width, while large bins obscure potentially useful information. For this reason, kernel density estimates (KDE) with 68% confidence intervals are plotted alongside histograms. A KDE is a method for estimating a continuous probability distribution from a finite set of sampled data points. The kernel was chosen to be equal to the measurements errors in opening angle as determined by the a study using a highly collimated  $^{60}\text{Co}$  source that was placed at different points along a detector. The resulting measurement errors are well-described by a gaussian with a sigma that varies with  $\theta_{nn}$  according to the data presented in Fig. 31. Mathematical details of the KDE method used in this work are outlined in ref [?].

Alongside each measurement is the result of a FREYA simulation with the exact same energy cuts applied. For  $^{238}\text{U}$ , there were a total of 2952 two-neutron coincident events after the subtraction of accidentals, and for  $^{252}\text{Cf}$ , there were a total of 21,882.

#### 4. RESULTS

---

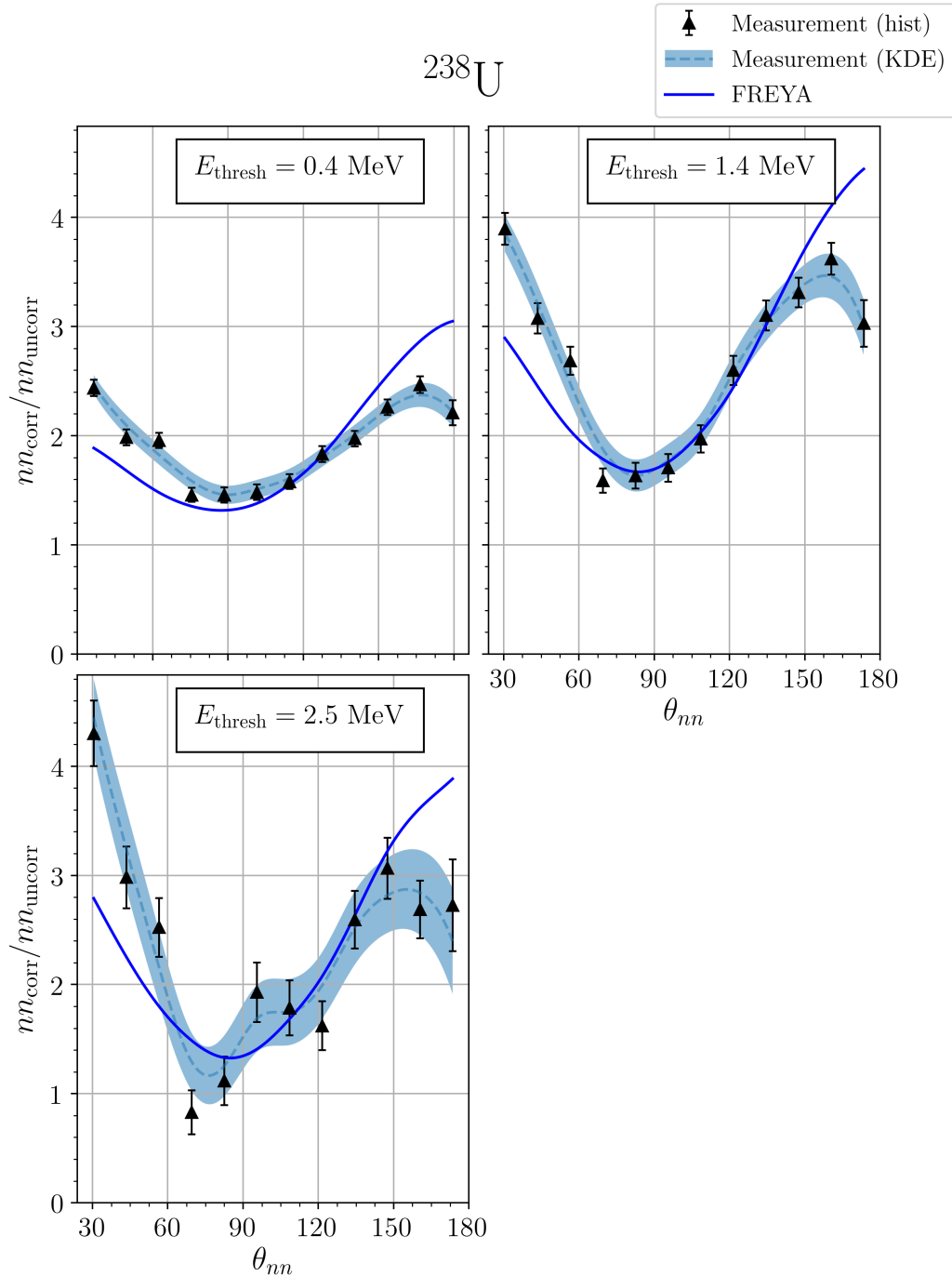


Figure 42:  $\theta_{nn}$  distribution with minimum energy threshold cuts applied to all neutrons. The number of events contributing to each plot are, starting from the lower left and moving clockwise: 314, 2952, and 1489

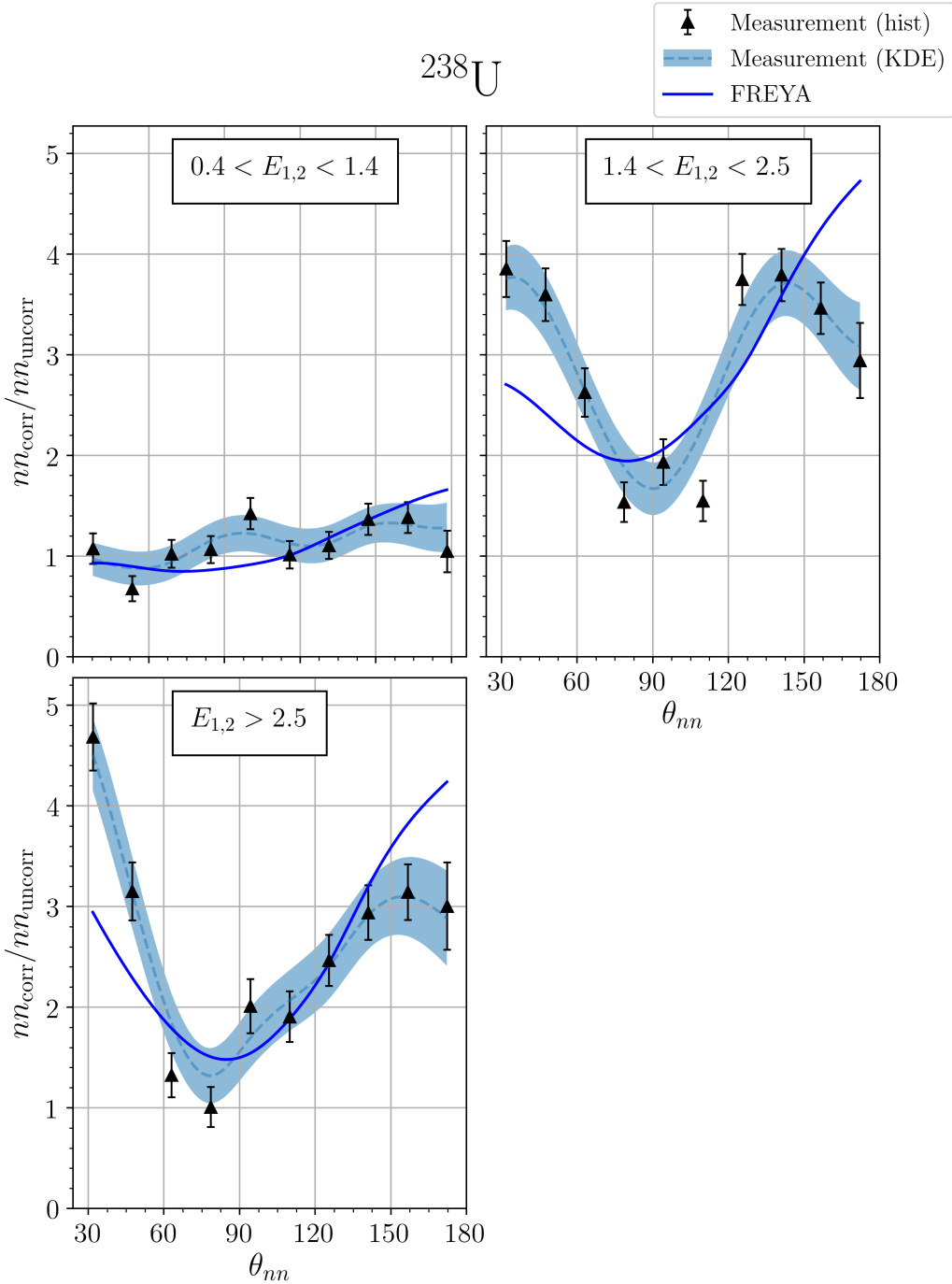


Figure 43:  $\theta_{nn}$  distribution with cuts requiring that the energy of both coincident neutrons be within the specified range. The number of events contributing to each plot are, starting from the lower left and moving clockwise: 303, 266, and 433.

#### 4. RESULTS

---

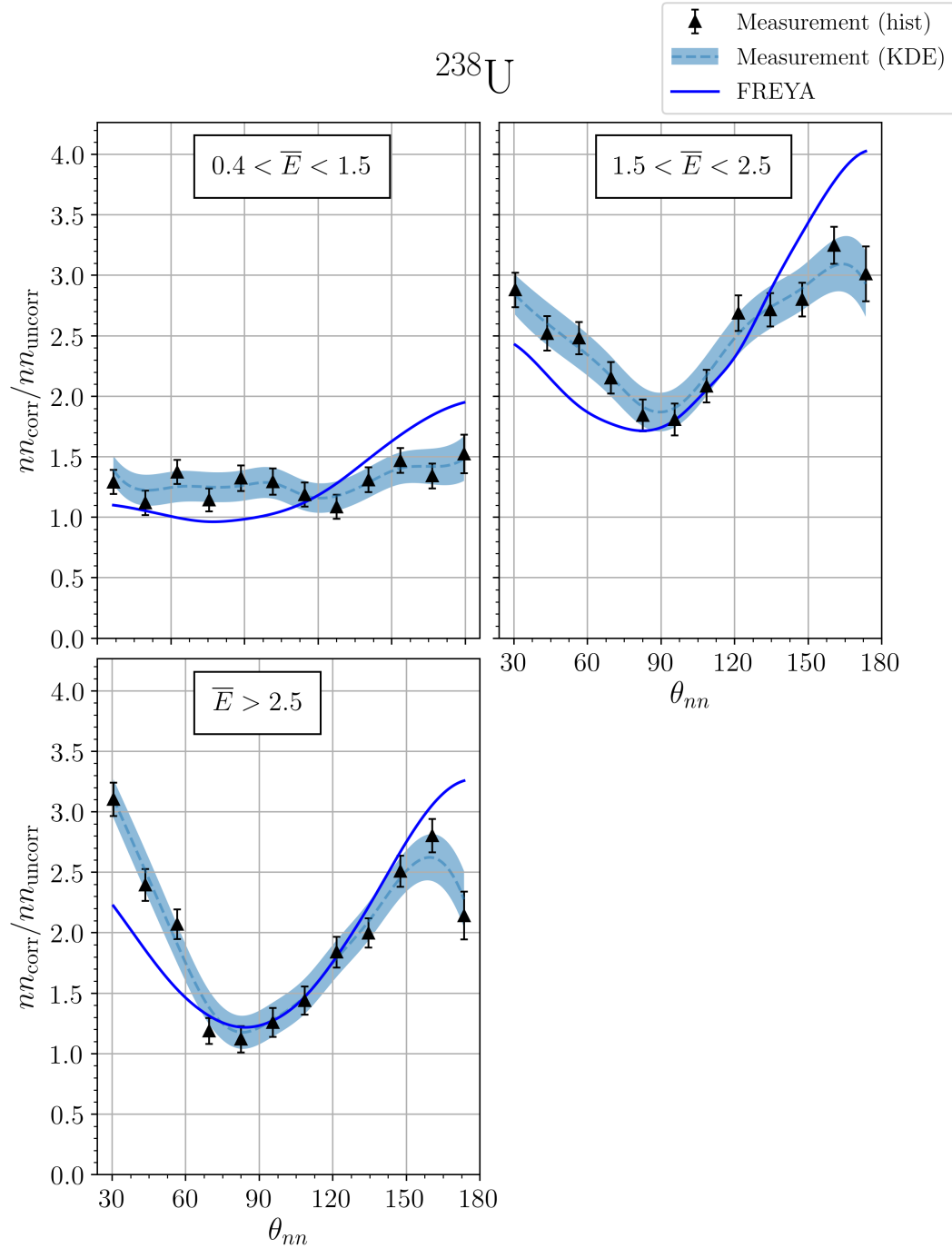


Figure 44:  $\theta_{nn}$  distribution with cuts on the mean energy ( $\bar{E}$ ) of the two coincident neutrons. The number of events contributing the each plot are, starting from the lower left and moving clockwise: 1009, 756, 1187

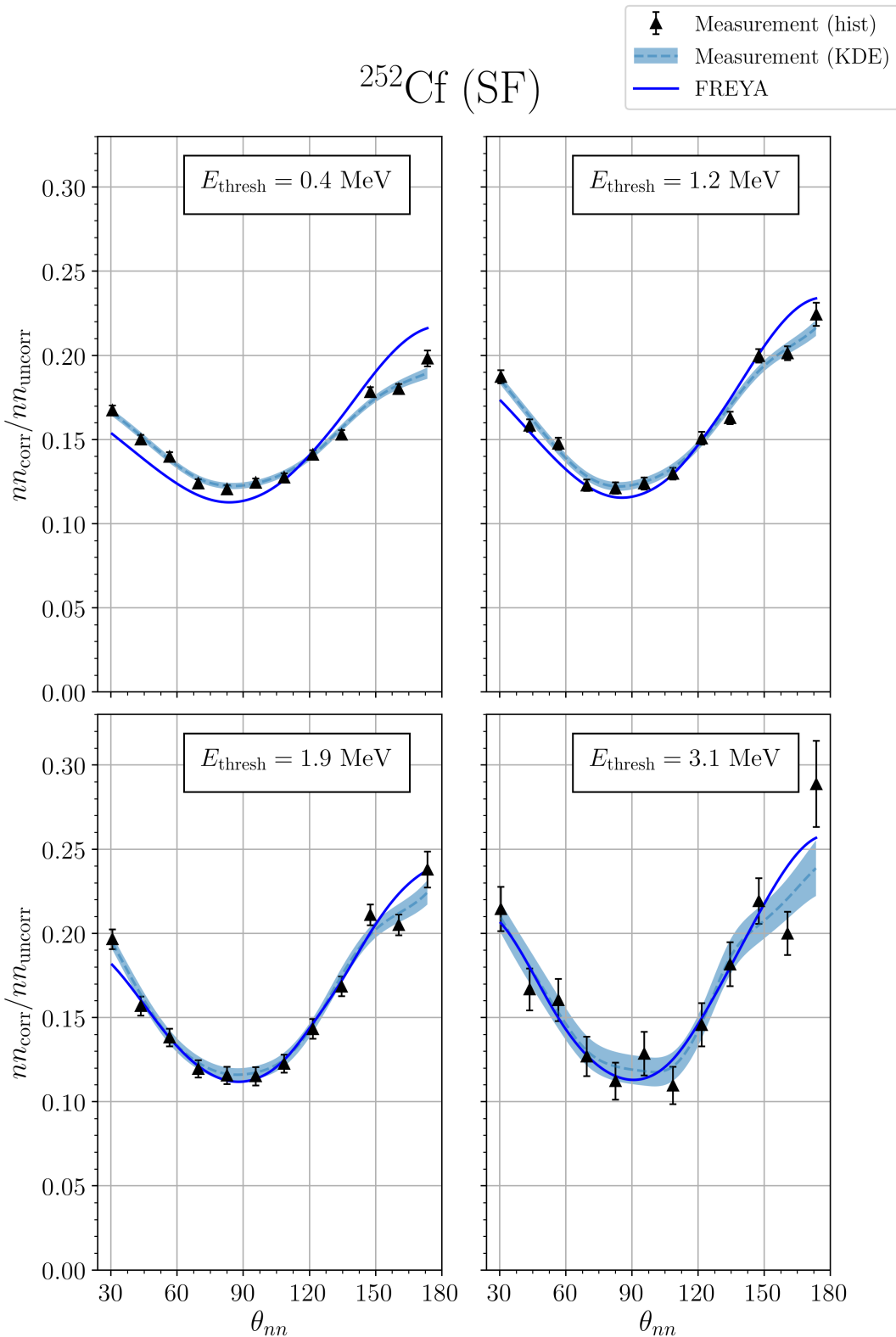


Figure 45:  $\theta_{nn}$  distribution a minimum energy threshold cuts applied to all neutrons. The number of events contributing the each plot are, starting from the lower left and moving clockwise: 21882, 12519, 5451, 1262

#### 4. RESULTS

---

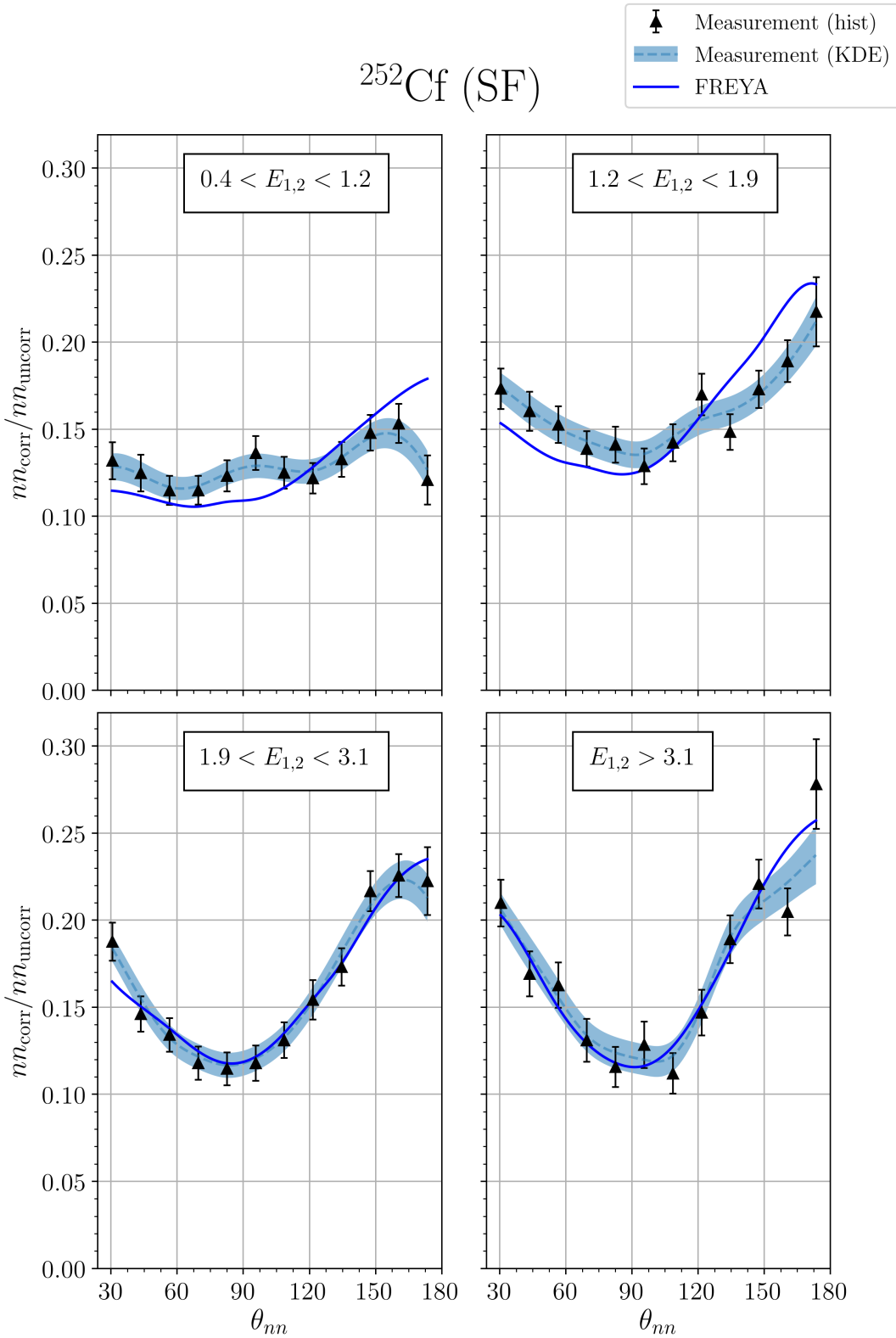


Figure 46:  $\theta_{nn}$  distribution with cuts requiring that the energy of both coincident neutrons be within the specified range. The number of events contributing to each plot are, starting from the lower left and moving clockwise: 1291, 1456, 1567, 1198

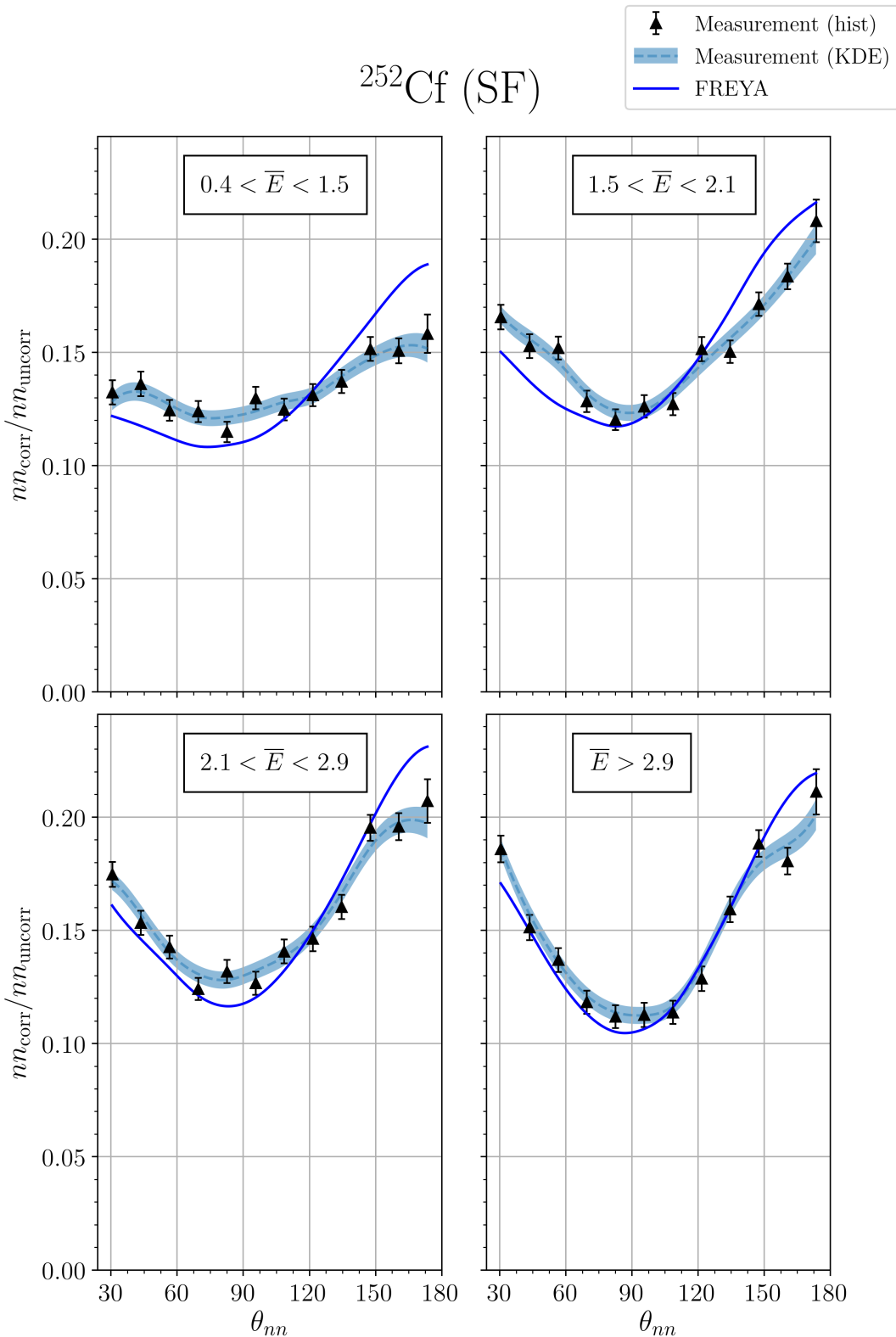


Figure 47:  $\theta_{nn}$  distribution with cuts on the mean energy ( $\bar{E}$ ) of the two coincident neutrons. The number of events contributing the each plot are, starting from the lower left and moving clockwise: 4974, 5947, 5908, 5053

## 4. RESULTS

---

### 4.3 Correlation of $\theta_{abs}$

While these results are consistent with the effect of the kinematic focusing of the neutrons due to the recoil of the fission fragments, the data show a marked decrease in the two-neutron opening angle correlation in the region from about  $165^\circ$  to  $180^\circ$ , which can be seen in Figs. 212 and 49, as well as in Figs 42 through 44. This feature is not evident in previous work on spontaneous and neutron induced fission. As previously discussed, photofission differs from spontaneous and neutron induced fission in that the fission fragments for the photon-induced reaction exhibit an asymmetry in their angle of emission, with the most likely orientation of the fission axis lying perpendicular to the direction of the incident photon. With this in mind, the following series of angular cuts were made on the data. Fig. 48 shows the distributions of absolute opening angles of the two-neutron events for three different cuts on the value of the two-neutron opening angle. For two-neutron opening angles between  $120^\circ$  and  $160^\circ$ , there is an increased preponderance of both neutrons being emitted around  $90^\circ$ , consistent with the interpretation of kinematic focusing of neutrons coming from fission fragments which are themselves being emitted preferentially at  $90^\circ$ . However, in the opening angle region where the two-neutron correlation is reduced, from about  $160^\circ$  to  $180^\circ$ , this feature is less prominent.

Furthermore, if one plots the opening angle distributions for the case in which at least one neutron is emitted perpendicular to the incident photon versus the case in which neither neutron is emitted perpendicular to the incident photon (Fig. 49), one sees that the two-neutron correlation is greatly reduced at  $180^\circ$  in opening angle when at least one of the neutrons is emitted along the preferred fission axis.

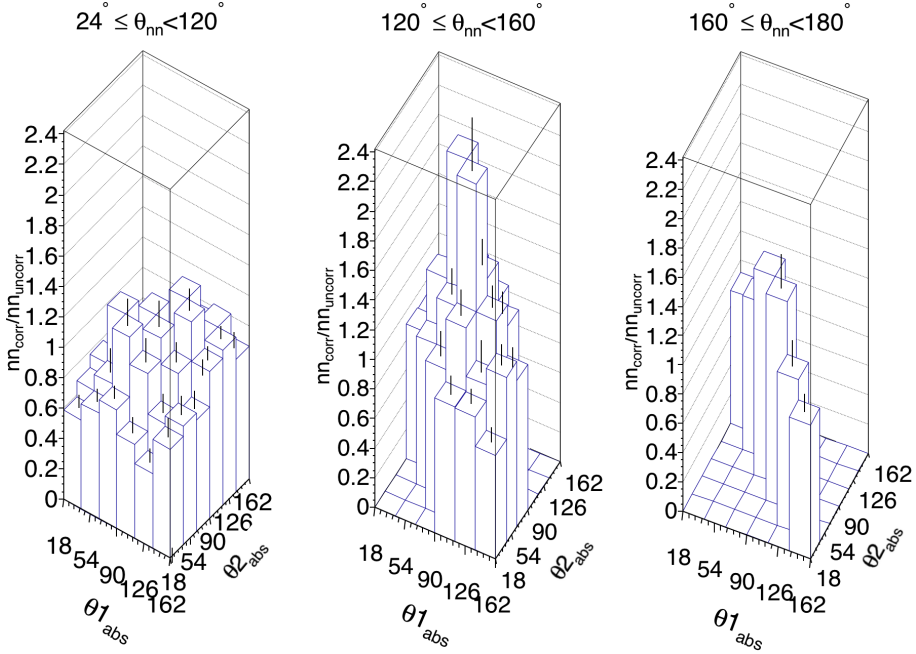


Figure 48: Correlation is shown between the angles of each neutron with respect to the incident photon beam, denoted by  $\theta_{1abs}$  and  $\theta_{2abs}$ . Empty bins exist because of incomplete  $\theta_{abs}$  coverage.

These data are consistent with two possible explanations. First, it is possible that there is a decrease in neutron emission along the fission axis. Second, the neutrons may indeed be emitted isotropically in the rest frame of the fission fragment, but one fragment essentially shadows the neutrons emitted from the other fragment, either through absorption or scattering. A definitive interpretation of this decreased two-neutron correlation for large opening angles in photo-fission requires further study.

## 4. RESULTS

---

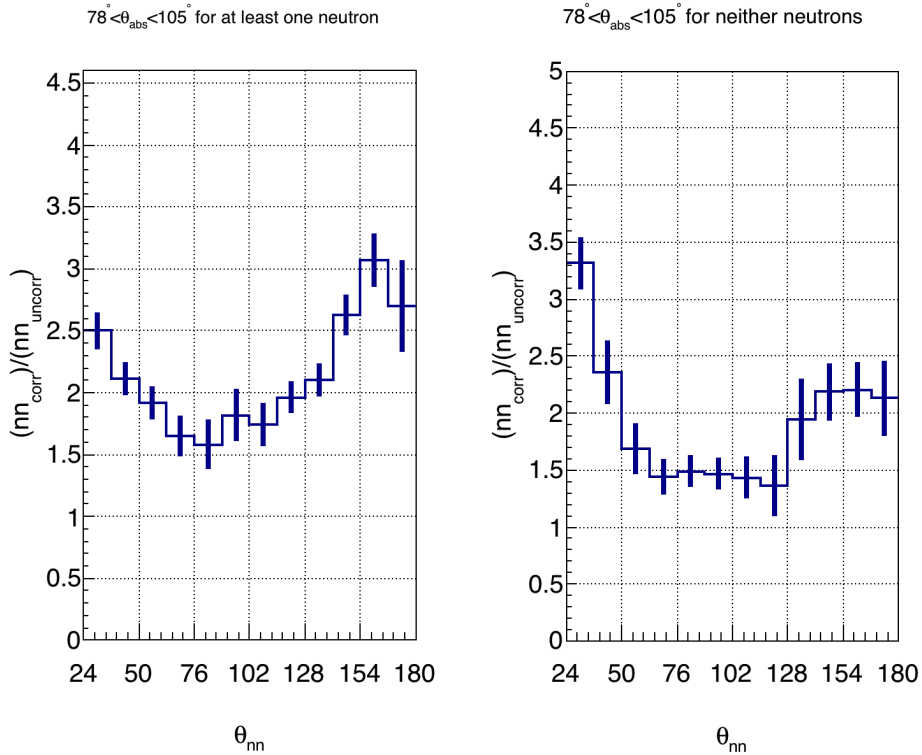


Figure 49: Requiring that at least one of the coincident neutrons be emitted nearly perpendicular to the photon beam (left) produces an opening angle distribution that is different from that produced when it is required that both neutrons are emitted nearly parallel to the photon beam (right).

### 4.4 Rates

Table 41 shows the rates, per pulse, of the detection of photons and neutrons for each detector. The overall rate of neutron singles and doubles was  $4.89 \times 10^{-3}$  and  $3.57 \times 10^{-5}$  per pulse, respectively.

---

<b>Detector</b>	<b>neutron rate</b>	<b>photon rate</b>	
30 bottom	4.43E-04	1.93	$\cdot 10^{-1}$
30 top	2.11E-04	1.68	$\cdot 10^{-1}$
54	5.03E-04	3.77	$\cdot 10^{-1}$
78	4.27E-04	9.67	$\cdot 10^{-2}$
102	3.61E-04	4.73	$\cdot 10^{-2}$
126	7.13E-04	5.14	$\cdot 10^{-2}$
150	5.76E-04	3.79	$\cdot 10^{-2}$
210	7.16E-04	4.99	$\cdot 10^{-2}$
234	4.49E-04	4.49	$\cdot 10^{-2}$
258	5.27E-04	5.90	$\cdot 10^{-2}$
282	4.42E-04	1.04	$\cdot 10^{-1}$
306	3.40E-04	3.17	$\cdot 10^{-1}$
330 bottom	3.46E-04	2.35	$\cdot 10^{-1}$
330 top	3.24E-04	2.50	$\cdot 10^{-1}$

Table 41: Per pulse rate of neutrons and photons on each detector. Only one particle can be detected by a given detector per pulse, so the rate of photon detection affects the measured neutron rate.



## Chapter 5

---

### Concluding Remarks

---

Two-neutron angular correlations in the photofission of  $^{238}\text{U}$  were measured using 10.5 MeV end-point bremsstrahlung photons produced via a low duty factor, pulsed linear electron accelerator. The measured angular correlations reflect the underlying back-to-back nature of the fission fragments. The method of analysis used a single set of experimental data to produce a opening angle distribution of correlated and uncorrelated neutron pairs. A ratio is taken between these two sets to provide a self-contained result of angular correlations, in that the result is independent of neutron detector efficiencies. Two-neutron angular correlation measurements were also made using neutrons from the SF of  $^{252}\text{Cf}$  and show good agreement with previous measurements.

Measured two-neutron opening angle correlations in the photofission of  $^{238}\text{U}$  do not agree very well with simulations using FREYA version 2.0.3, which uses a neutron-induced model to approximate photofission. These data will be useful for fine-tuning the photofission models that will be incorporated into future versions of FREYA.

An anomaly was observed in the rate of neutron emission at opening angles near  $180^\circ$ , in which diminished rates resulted in a local maximum at about

## 5. CONCLUDING REMARKS

---

$160^\circ$  instead of the expected  $180^\circ$ , as seen in all past measurements of neutron-induced and spontaneous fission. We offer two possible explanations for this effect: (i) There is a decrease in neutron emission along the fission axis, or (ii) the neutrons may indeed be emitted isotropically in the rest frame of the fission fragment, but one fragment essentially shadows the neutrons emitted from the other fragment, either through absorption or scattering. A definitive interpretation of this decreased two-neutron correlation for large opening angles in photo-fission requires further study.

---

## Bibliography

---

- [1] Harry R. Bowman, Stanley G. Thompson, J. C. D. Milton, and Wladyslaw J. Swiatecki. Velocity and angular distributions of prompt neutrons from spontaneous fission of Cf<sup>252</sup>. *Phys. Rev.*, 126:2120–2136, Jun 1962.
- [2] C. Budtz-JÃžrgensen and H.-H. Knitter. Simultaneous investigation of fission fragments and neutrons in 252Cf (SF). *Nuclear Physics A*, 490(2):307 – 328, 1988.
- [3] J. T. Caldwell, E. J. Dowdy, R. A. Alvarez, B. L. Berman, and P. Meyer. Experimental determination of photofission neutron multiplicities for 235U, 236U, 238U, and 232Th using monoenergetic photons. *Nuclear Science and Engineering*, 73(2):153–163, 1980.
- [4] S. D. Clarke, B. M. Wieger, A. Enqvist, R. Vogt, J. Randrup, R. C. Haight, H. Y. Lee, B. A. Perdue, E. Kwan, C. Y. Wu, R. A. Henderson, and S. A. Pozzi. Measurement of the energy and multiplicity distributions of neutrons from the photofission of <sup>235</sup>U. *Phys. Rev. C*, 95:064612, Jun 2017.
- [5] Kyle Cranmer. Kernel estimation in high-energy physics. *Computer Physics Communications*, 136(3):198–207, 2001.

## BIBLIOGRAPHY

---

- [6] S. Debenedetti, J. E. Francis, W. M. Preston, and T. W. Bonner. Angular dependence of coincidences between fission neutrons. *Phys. Rev.*, 74:1645–1650, Dec 1948.
- [7] A. M. Gagarski, I. S. Guseva, V. E. Sokolov, G. V. Val'Ski, G. A. Petrov, D. O. Krinitzin, D. V. Nikolaev, T. A. Zavarukhina, and V. I. Petrova. Neutron-neutron angular correlations in spontaneous fission of  $^{252}\text{Cf}$ . *Bulletin of the Russian Academy of Sciences, Physics*, 72:773–777, July 2008.
- [8] Jefferson Lab. CODA 2.6, 2015.
- [9] Krishichayan, M. Bhike, A. P. Tonchev, and W. Tornow. Fission product yield measurements using monoenergetic photon beams. In *European Physical Journal Web of Conferences*, volume 146 of *European Physical Journal Web of Conferences*, page 04018, September 2017.
- [10] Lawrence Berkeley National LaboratoryLawrence Livermore National LaboratoryLos Alamos National LaboratoryUniversity of Michigan Nuclear Engineering. FREYA 2.0.3, 2016.
- [11] Matthew J. Marcath, Tony H. Shin, Shaun D. Clarke, Paolo Peerani, and Sara A. Pozzi. Neutron angular distribution in plutonium-240 spontaneous fission. *Nuclear Instruments and Methods in Physics Research, Section A: Accelerators, Spectrometers, Detectors and Associated Equipment*, 830:163–169, 9 2016.
- [12] Eric C. Miller, Shaun D. Clarke, Marek Flaska, Sara A. Pozzi, and Enrico Padovani. MCNPX-PoliMi post-processing algorithm for detector response simulations. *JNMM, Journal of the Institute of Nuclear Materials Management*, 40(2):34–41, 12 2012.

---

## Bibliography

- [13] S Nair, D B Gayther, B H Patrick, and E M Bowey. Fission-neutron and fragment angular distributions from threshold photofission of  $^{232}\text{Th}$  and  $^{238}\text{U}$ . *Journal of Physics G: Nuclear Physics*, 3(7):965, 1977.
- [14] G. A. Petrov. Current status of the search for scission neutrons in fission and estimation of their main characteristics. *AIP Conference Proceedings*, 798(1):205–212, 2005.
- [15] Sara A Pozzi, Enrico Padovani, and Marzio Marseguerra. MCNP-PoliMi: a Monte-Carlo code for correlation measurements. *Nuclear Instruments and Methods in Physics Research Section A: Accelerators, Spectrometers, Detectors and Associated Equipment*, 513(3):550 – 558, 2003.
- [16] Sara A. Pozzi, Brian Wieger, Andreas Enqvist, Shaun D. Clarke, Marek Flaska, Matthew Marcath, Edward Larsen, Robert C. Haight, and Enrico Padovani. Correlated neutron emissions from  $^{252}\text{Cf}$ . *Nuclear Science and Engineering*, 178(2):250–260, 2014.
- [17] J. S. Pringle and F. D. Brooks. Angular correlation of neutrons from spontaneous fission of  $^{252}\text{Cf}$ . *Phys. Rev. Lett.*, 35:1563–1566, Dec 1975.
- [18] V. E. Sokolov and G. A. Petrov. Investigation of the angular dependences of neutron-neutron coincidences from  $^{252}\text{Cf}$ ,  $^{235}\text{U}$ ,  $^{233}\text{U}$  and  $^{239}\text{Pu}$  fission in search of scission neutrons. *Proc. XVIII Internat. Seminar on Interaction of Neutrons with Nuclei (ISSIN-18)*, pages 108–118, 2010.
- [19] P. Talou, R. Vogt, J. Randrup, M. E. Rising, S. A. Pozzi, J. Verbeke, M. T. Andrews, S. D. Clarke, P. Jaffke, M. Jandel, T. Kawano, M. J. Marcath, K. Meierbachtol, L. Nakae, G. Rusev, A. Sood, I. Stetcu, and C. Walker.

## BIBLIOGRAPHY

---

- Correlated prompt fission data in transport simulations. *The European Physical Journal A*, 54(1):9, Jan 2018.
- [20] J. M. Verbeke, L. F. Nakae, and R. Vogt. Neutron-neutron angular correlations in spontaneous fission of  $^{252}\text{Cf}$  and  $^{240}\text{Pu}$ . *Phys. Rev. C*, 97:044601, Apr 2018.